TURUN YLIOPISTON JULKAISUJA
ANNALES UNIVERSITATIS TURKUENSIS

SARJA - SER. A I OSA - TOM. 460

ASTRONOMICA - CHEMICA - PHYSICA - MATHEMATICA

Theoretical Modelling and Experimental Studies of Synchrotron Radiation Induced Molecular Dissociation Processes

by

Dang Trinh Ha

TURUN YLIOPISTO
UNIVERSITY OF TURKU
Turku 2013

From

Department of Physics and Astronomy
University of Turku
Turku, Finland

Superviser

Doctor Sari Granroth
Dept. of Physics and Astronomy
University of Turku
Turku, Finland

Research Director

Professor Edwin Kukk
Dept. of Physics and Astronomy
University of Turku
Turku, Finland

Reviewers

Docent Sami Heinäsmäki
Department of Physics
University of Oulu
Oulu, Finland

Asst. Professor Osamu Takahashi
Department of Chemistry
Hiroshima University
Hiroshima, Japan

Opponent

Professor Kiyoshi Ueda
Institute of Multidisciplinary Research for Advanced Materials
Tohoku University
Sendai, Japan

ISBN 978-951-29-5347-9 (PRINT)
ISBN 978-951-29-5348-6 (PDF)
ISSN 0082-7002
Painosalama Oy – Turku, Finland 2013

Con kính tri ân Ba Má.

Acknowledgements

A thousand mile journey begins with a single step, said a Chinese philosopher. Even though this work has been a very long journey from my point of view, the first steps were quite simple thanks to Docent Jarkko Leiro and Professor Edwin Kukk. The remaining part of the journey was significantly relieved by many people who have aided me in bringing the thesis to this point.

The very first step was Jarkko Leiro's agreement to take me on as a summer employee to do research in the Materials Science group - I thank him. Next, I am deeply indebted to Edwin Kukk for accepting and funding me as a Ph.D. student. And no less importantly, he directed me along this journey and taught me numerous scientific skills, without which this thesis would not exist. I'd like to thank Doctor Sari Granroth for being helpful and for guiding me in this work. The collaboration with Doctors Kuno Kooser and Eero Itälä is gratefully acknowledged. Their efforts were undoubtedly essential contributions to this work. Also, I am obliged to Eero Itälä for introducing me to a subspecies of Finnish humour. In addition to the aforementioned people, Markku Heinonen, Taina Laiho and Helena Levola have made the Materials Science group a cosy second home.

Besides the University of Turku, research has sometimes taken me to MAX-lab where I have fortunately had the chance to collaborate with many great people such as Professors Elisabeth Rachlew and Ergo Nõmmiste, Docent Marko Huttula, and Doctors Michael Huels and Samuli Urpelainen. Also, the staff of the

MAX-lab has been extremely helpful. In addition, a trip to University of Oulu four years ago furnished me with two saviours, Doctors Minna Patanen and Antonio Caló, who helped me to get started with GAMESS software. Lastly, I am very lucky to know Professors Manuel Alcamí and Fernando Martín, and Doctors Yang Wang and Pablo López-Tarifa for they led me to the wonderland of molecular dynamics. I thank them all.

I want to express my gratitude to the pre-examiners, Assistant Professor Osamu Takahashi and Docent Sami Heinäsmäki, for their constructive comments which improved the quality of this thesis. I am also greatly honoured to have Professor Kiyoshi Ueda as my opponent at the doctoral defence.

The financial support from the Academy of Finland, Magnus Ehrnrooth Foundation (n:o fy2011n15), Turku University Foundation (n:o 7946 and n:o 8768) and Väisälä Foundation are gratefully acknowledged. I'd like to thank University of Oulu, the Magerit CeSVima and the Pleione team for computing resources.

Finally, I'd like to convey my thanks to Soile and every other member of my big family and all my friends for not only being patient but also for encouraging, supporting and energizing me to proceed on this journey. Especially, I'd like to thank Soile one billion times for translating my work written in a non-human readable language into understandable English.

Abstract

In this thesis, synchrotron radiation induced fragmentation of selected small molecules was studied by means of energy-resolved photoelectron photo-ion coincidence technique and computational quantum chemistry methods. The measurements were performed on gas phase molecules acrylonitrile (C_3H_3N), thymine ($C_5H_6N_2O$), uracil ($C_4H_4N_2O_2$), 5-Bromouracil ($C_4H_3BrN_2O_2$), D-ribose ($C_5H_{10}O_5$), 2-deoxy-D-ribose ($C_5H_{10}O_4$), methionine ($C_5H_{11}NO_2S$) and selenium (Se_n) microclusters. The *ab initio* methods applied in the research include Hartree-Fock, post Hartree-Fock, density functional theory, time-dependent density functional theory (TDDFT), TDDFT-based Ehrenfest molecular dynamics, Born-Oppenheimer molecular dynamics and Car-Parrinello molecular dynamics. The principal contribution of the author is in theoretical modelling and experimental data analysis.

Contents

List of papers

This thesis consists of the introductory review part and the following research papers [12, 17, 18, 22, 23]

I Itälä, E.; Ha, D. T.; Kooser, K.; Rachlew*, E.; Huels*, M. & Kukk, E. 2010: *Fragmentation patterns of core ionized thymine and 5-bromouracil.* - J. of Chem. Phys. 133(15): 154316. [A1]

II Kooser, K.; Ha, D. T.; Granroth, S.; Itälä, E.; Partanen*, L.; Nõmmiste*, E.; Aksela*, H. & Kukk, E. 2010: *Resonant Auger electron-photoion coincidence study of the fragmentation dynamics of acrylonitrile molecule.* - J. of Phys. B: AMO Physics 43(23): 235103. [A1]

III Itälä E.; Ha D.T.; Kooser K.; Nõmmiste* E.; Joost* U. & Kukk E. 2011: *Fragmentation patterns of core ionized uracil.* - Int. J. Mass Spectrom. 306(1), p.82-90. [A1]

IV Ha D. T.; Huels* M. A.; Huttula* M.; Urpelainen* S. and Kukk E. 2011: *Experimental and ab initio study of the photofragmentation of DNA and RNA sugars.* - Physical Review A 84(3). [A1]

V Kooser K.; Ha D. T.; Itälä E.; Laksman* J.; Urpelainen* S. and Kukk E. 2012: *Size selective spectroscopy of Se microclusters.* -Journal of Chemical Physics 137(4), 044304. [A1]

VI Ha D. T.; Wang Y.; Alcamí M.; Itälä E.; Kooser K.; Urpelainen S.; Huels M. A.; Kukk E. and Martín F.: *Fragmentation Dynamics of Doubly Charged Methionine in the Gas Phase.* -Physical Review A *Submitted March 2013.*

The author is the principal writer of Papers IV & VI, where he has performed the *ab initio* calculations, participated in the measurements and analysed the experimental data. In addition, the author has participated in the measurements, performed the *ab initio* calculations and written computational parts contributing to Papers I-III & V. The author has also written a minor program code for generating initial geometries of a given set of atoms for optimization in order to find the geometry of the lowest total energy in Papers I-III & V.

In addition, the author has participated in the research papers below, but they are not included in this thesis.

1 Itälä, E.; Kukk, E.; Ha, D. T.; Granroth, S.; Calo*, A.; Partanen*, L.; Aksela*, H. & Aksela*, S. 2009: Fragmentation patterns of doubly charged acrylonitrile molecule following carbon core ionization. - Journal of Chemical Physics 131(11): 114314. [A1]

2 Kukk, E.; Kooser, K.; Ha, D. T.; Granroth, S. & Nõmmiste*, E. 2010: *VUV-induced dissociation of methylchlorosilanes, studied by electronion coincidence spectroscopy.* - Journal of Physics B: Atomic, Molecular and Optical Physics 43(6): 065103. [A1]

Chapter 1

Introduction

Interaction between light – described in modern physics as electromagnetic waves or as quanta of energy – and matter has always fascinated the human kind. Different materials of specific size, shape and chemical composition respond to light of a certain frequency in different ways such as light refraction, light scattering or light absorption. Today, each interaction type has its own research interests, but photoabsorption may be the most studied one due to its mechanism and the wide variety of phenomena resulting from absorption.

Molecular fragmentation, one of the phenomena can follow the absorption of light ranging from vacuum ultraviolet (VUV) to X-ray has become a very popular research subject along with the development of synchrotron radiation sources during the past half century. Yet, we don't thoroughly understand how a given quantum of energy delivered to a molecular system may eventually cause it to crumble into certain fragments. The more degrees of freedom a molecular system has, the larger variety of possible dissociation channels it may possess. The observables we obtain from measurements often reveal only a distribution of the most probable channels and the less likely channels are sometimes drowned under background noise. Fortunately, it is often exactly the answer to the question "Why are these the main channels?", that provides us important insight into the issue of synchrotron radiation induced molecular dynamics and fragmentation.

Understanding the fragmentation mechanisms of a studied system not only reveals the physics concealed behind the specific system itself but it may also shed light onto photofragmentation processes in general. Furthermore, the capability of cutting certain chemical bonds resulting in desired fragments would bring interesting applications into both science and industry. The ability to produce desired fragments from a specific parent compound by photochemistry is certainly appealing, although the production alternative may not be the most economic one. For example, the capability of controlling toxic radicals in radiation therapy while performing cancer treatments is a very important advance in radiobiology.

In this thesis we attempt to understand molecular fragmentation induced by VUV and soft X-ray light by means of energy-resolved photoelectron photo-ion coincidence (PEPICO) technique with synchrotron radiation as the tunable light source. In parallel, the study was also conducted by using different computational quantum chemistry methods. Comparing theoretical results with experimental data may bring us firm findings and a versatile outlook on the topic.

The thesis is organized into five chapters. The 'Introduction' chapter shows the motivation for this work, and the second chapter 'Light-matter interaction' presents the underlying fundamental mechanisms leading to photo-fragmentation. The third chapter 'Experimental method' provides a description of the essential apparatus, experimental setup and how the experimental data is analysed. The fourth chapter '*Ab initio* methods' overviews the computational quantum chemistry methods behind the software [11, 40, 45] used in the research. The final chapter 'Results and conclusions' is devoted to summarizing the research papers and cogitating what we have learnt from the research.

Chapter 2

Light-matter interaction

A prerequisite for comprehending synchrotron radiation induced molecular dissociation is to understand, first of all, how photoabsorption changes the electronic structure of a molecular system. A most suitable tool for this end is electron spectroscopy. It can be considered to have a foundation in the fundamental works of Hertz [14] in 1887 and Einstein in 1905 [9] concerning photoelectric effect.

Having interacted with an incident photon, the system may undergo internal bond breakage if the modification of the electronic structure necessitates that. In general, photoabsorption always induces nuclear motions either as changes in bond lengths and angles, isomerisation, or fragmentation. In this thesis, we concentrate on the latter outcome. The molecules studied here are organic compounds (and, in one publication, clusters). While they can by no means be considered as large molecules, they nevertheless already exhibit such a variety of dissociation pathways to make a comprehensive modelling a formidable task.

In this chapter we highlight a few characteristic interaction types between photon and electronic structures in Section 2.1 and 2.2. In addition, multi-body fragmentation mechanisms are surveyed in Section 2.3.

2.1 Electronic structure

Electron in an atomic or molecular system cannot be represented as a point charge but rather as a wave in a confined space in the vicinity of a nuclear centre by using a quantum mechanical wave function [36]. A wave function describing an electron in an atom can also be referred to as a *spin-orbital*, whereas a *spin molecular orbital* refers to a wave function describing an electron in a molecule.

Each electronic state of an atom is defined by four different quantum numbers (n, l, m_l, m_s). The first three quantum numbers (n, l, m_l) define three-dimensional spatial related variables defining the probability of finding an electron in a region of an atom. The principal quantum number $n = 1, 2, 3..$ relates to the size of an orbital, and the orbital angular momentum quantum number $l = 0, 1, .., n-1$ (corresponding to $l = s, p, d, f..$) defines the shape of an orbital. The orbital magnetic momentum number $m_l = -l, .., 0, .., l-1, l$ defines the orientation of an orbital in a magnetic field. The fourth quantum number, a spin magnetic quantum number $m_s = \pm{}^1/_2$ defines the spin orientation of an electron in a given orbital [33]. The electronic structure of an atom can be described as electron configuration, which shows how electrons are distributed in the orbitals. For example, the electron configuration of an oxygen atom in the ground state is $1s^2 2s^2 2p^4$.

A spatial molecular orbital (MO) is commonly represented as a linear combination of (spatial) atomic orbitals (AO) [19, 26], and labelling MOs is different than in the case of atoms. MOs are named according to the interaction type of the constituent AOs. They can be categorized by MO symmetry (σ, π *etc.*) and also by whether the interaction is constructive (bonding) or destructive (non-bonding). A MO posing σ symmetry is symmetrical with respect to the internuclear axis, and it results from the interaction of two s- or p_z-type AOs. A MO posing π symmetry is asymmetrical with respect to the rotation around the internuclear axis, and it is a result of the interaction of two p_x- or p_y-type AOs. Additionally, centrosymmetric molecules (*e.g.* a homonuclear molecule X_2 is, but a heteronuclear one XY

is not) are further classified as either *gerade* (g) or *ungerade* (u) symmetry. A MO has gerade symmetry if inversion through the centre of symmetry in a molecule does not change the sign of the MO. Conversely, a MO is said to be ungerade if the inversion operation changes the sign of the MO. For example, the electron configuration of oxygen molecule O_2 in the electronic ground state is $1\sigma_g^2 1\sigma_u^2 2\sigma_g^2 2\sigma_u^2 3\sigma_g^2 1\pi_u^4 1\pi_g^2$ (unpaired electrons with $m_s = +^1/_2$ in the MO $1\pi_g^2$). Quantum mechanically, a molecular orbital can be represented in terms of atomic orbitals $\Psi_{MO} = \sum_i c_i \Phi_i$, where an atomic orbital Φ_i contributing to the MO is weighted according to the coefficient c_i. Several methods determining the coefficients c_i will be discussed later in Chapter '*Ab initio* methods'.

Generally, orbitals are categorized into three classes: core, valence, and unoccupied (or virtual) orbitals. Core orbitals are energetically low (in negative value) and typically tightly localized at a nucleus/nuclei such as the MOs $1\sigma_g^2$ and $1\sigma_u^2$ in an oxygen molecule O_2 (see Figure 2.1), because core electrons are subjected to strong attractive Coulomb force with the nearest nucleus. Valence orbitals are in higher energy levels and they character-

Figure 2.1: Core molecular orbitals of oxygen molecule O_2: a) the $1\sigma_g^2$ orbital and b) the $1\sigma_u^2$ orbital. The "+" and "-" characters are orbital signs.

ize chemical properties of an atom or a molecule, because loosely bound electrons occupying the valence orbitals may flexibly interact with valence electrons of another atomic or molecular system. A valence MO of special significance is the highest occupied molecular orbital (HOMO) due to its description of the least tightly bound electron [36] (see the HOMO of oxygen molecule in Figure 2.2). Moreover, the energy level of the HOMO can act as an approximation for predicting the first ionization potential of the molecule. Virtual orbitals are energetically above valence orbitals, and they can temporarily hold electrons promoted beyond valence levels in

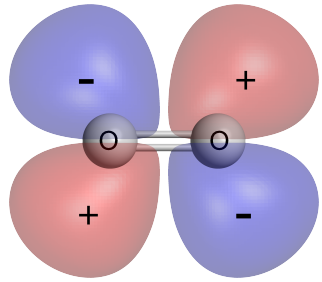

Figure 2.2: The highest occupied molecular orbital (HOMO, the $1\pi_g^2$ orbital) of oxygen molecule O_2. The "+" and "-" characters are orbital signs.

an excited system or accept additional electrons from an external system. Almost as significant as the HOMO, the energy of the lowest unoccupied molecular orbital (LUMO) belonging to the virtual orbital class can be used to estimate electron affinity of certain molecules [36]. In large systems, the HOMO-LUMO gap evolves into the band gap. Figure 2.3 shows the LUMO of oxygen molecule.

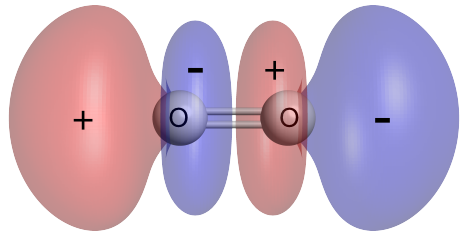

Figure 2.3: The lowest unoccupied molecular orbital (LUMO, the $3\sigma_u$ orbital) of oxygen molecule O_2. The "+" and "-" characters are orbital signs.

2.1.1 Potential energy surfaces

The electronic structure of a molecular system is not solely determined by the electrons but also by the charge and the position of the nuclei. Various nuclear configurations of a molecular system in a certain electronic state pose different total energies, which are the points forming the *potential*

energy surface (PES) relating to the given electronic state.

A diatomic molecule has a one-dimensional PES (in a two-dimensional (2D) space: energy *vs.* internal distance) for each electronic state. In more complex cases, a non-linear molecule built from at least three ($N \geq 3$) atoms poses a $(3N - 6)$ PES in every electronic state. The equilibrium geometry of a molecule in its electronic ground state represents a (local) minimum point on the surface associated with that state. Other stationary points, if present, represent different molecular conformations in either an equilibrium or a transition state. The number of such points can grow quickly as the size of a molecule increases. In addition to that, every excited or ionized state has its own PES associated with it. Certain PESs are *bound* and the remaining ones are *unbound* leading to fragmentation [36], but both kinds can become topologically very complex. Therefore, tracking every single dissociation pathway on PESs would not necessarily be the best strategy to study the fragmentation of a system. Fortunately, only a fraction of these channels define the dominant fragmentation schemes for a given system. Furthermore, different fragmentation mechanisms can be categorized into a few classes relieving the fragmentation analysis tasks.

2.2 Photoabsorption and relaxation processes

As mentioned earlier, photoabsorption changes the electronic structure of the interacting system according to the electronic structure and the photon energy. Here, we will discuss various interaction mechanisms induced by photoabsorption that are essential in this research.

2.2.1 Absorption by valence electrons

Absorbing photon energy equating to the energy difference of the total energies between the ground state and an excited state of the interacting system lifts a valence electron to a bound orbital:

$$h\nu + S \rightarrow S^*, \tag{2.1}$$

where $h\nu$ is photon energy, S represents the electronic ground state of an atomic or molecular system and S^* is an excited state of the system. For example, excitation of an oxygen molecule can involve lifting an electron from a valence orbital $\mathbf{1\pi_u}$ to the HOMO $\mathbf{1\pi_g}$ (e.g. from the electronic ground state $^3\Sigma_g^-$ to an excited state $^3\Sigma_u^-$):

$$h\nu_1 + 1\sigma_g^2 1\sigma_u^2 2\sigma_g^2 2\sigma_u^2 3\sigma_g^2 \mathbf{1\pi_u^4 1\pi_g^2} \longrightarrow 1\sigma_g^2 1\sigma_u^2 2\sigma_g^2 2\sigma_u^2 3\sigma_g^2 \mathbf{1\pi_u^3 1\pi_g^3},$$

where orbitals in boldface characters are the interacting orbitals.

Instead of excitation, absorbing photon energy may ionize a valence electron provided that the photon energy is higher than the binding energy of the valence electron:

$$h\nu + S \rightarrow S^+ + e_p^-, \tag{2.2}$$

where e_p^- is photoelectron and S^+ is singly charged state of the system S. For example, ionization from the valence orbital $\mathbf{3\sigma_g}$ of an oxygen molecule can promote the molecule to an unstable singly charged state:

$$h\nu_3 + 1\sigma_g^2 1\sigma_u^2 2\sigma_g^2 2\sigma_u^2 \mathbf{3\sigma_g^2} 1\pi_u^4 1\pi_g^2 \longrightarrow 1\sigma_g^2 1\sigma_u^2 2\sigma_g^2 2\sigma_u^2 \mathbf{3\sigma_g^1} 1\pi_u^4 1\pi_g^2 + e_p^-.$$

Having interacted accordingly with the absorbed photon energy, the promoted system (S^* or S^+) can subsequently relax to a lower energy state via either a radiative or isomerisation process in the case of the low relaxation energy release. It may take femtoseconds to picoseconds or even longer [4] for the system to relax to its ground state.

2.2.2 Absorption by core electrons

The major interest of this research is to study molecular fragmentation followed by core electron excitation and ionization. To this aim, various Auger processes [3] shall be reviewed here.

First consider a case where photoabsorption renders a system excited,

in which a core electron is elevated to a bound (unoccupied) orbital:

$$h\nu + S \xrightarrow[excitation]{core} S^*.$$

The core-excited state S^* is extremely unstable and the system may experience a relaxation process, in which an electron from a higher energy level falls to fill the core hole releasing energy. The energy may be released via radiative processes. However, in lighter chemical elements, the released energy is used to ionize another electron, the *Auger electron* (e_A^-), from an orbital energetically possible for ionization. The whole photoexcitation - *resonant Auger decay process* can generally be sketched as below:

$$h\nu + S \xrightarrow[excitation]{core} S^* \xrightarrow[ionization]{auto-} S^+ + e_A^- \tag{2.3}$$

The next example demonstrates a resonant Auger process concerning an oxygen molecule, where an electron is promoted from the core orbital $\mathbf{1}\sigma_\mathbf{u}$ to the HOMO $\mathbf{1}\pi_\mathbf{g}$ (e.g. from an electronic state $^1\Sigma_g^+$ to a state $^1\Pi_u$):

$$\begin{aligned} h\nu_4 + 1\sigma_g^2\mathbf{1}\sigma_\mathbf{u}^\mathbf{2}2\sigma_g^2 2\sigma_u^2 3\sigma_g^2 1\pi_u^4 \mathbf{1}\pi_\mathbf{g}^\mathbf{2} &\xrightarrow[excitation]{core} 1\sigma_g^2\mathbf{1}\sigma_\mathbf{u}^\mathbf{1}2\sigma_g^2 2\sigma_u^2 3\sigma_g^2 1\pi_u^4 \mathbf{1}\pi_\mathbf{g}^\mathbf{3} \\ &\xrightarrow[ionization]{auto-} 1\sigma_g^2\mathbf{1}\sigma_\mathbf{u}^\mathbf{2}2\sigma_g^2\mathbf{2}\sigma_\mathbf{u}^\mathbf{1}3\sigma_g^2 1\pi_u^4 \mathbf{1}\pi_\mathbf{g}^\mathbf{2} + e_A^-. \end{aligned}$$

If photoabsorption results in the ionization of a core electron of a system, the interacting system may undergo *normal Auger decay process* which resembles *resonant Auger decay process*. Here, the cationic excited system S^{*+} relaxes in such a way that the hole in a subshell is filled by an electron from an outer shell and the released energy associated with the decay process is high enough to ionize a secondary (Auger) electron leaving the system doubly charged. Thus, interaction process beginning from the neutral state can be sketched as below:

$$h\nu + S \xrightarrow[ionization]{core} S^{*+} + e_p^- \xrightarrow[ionization]{auto-} S^{++} + e_p^- + e_A^- \tag{2.4}$$

Again, an oxygen molecule exemplifies a normal Auger process, in which ionization from the core orbital $\mathbf{1}\sigma_\mathbf{u}$ is followed by normal Auger decay

process involving the valence orbitals $\mathbf{1\pi_u}$ and $\mathbf{1\pi_g}$:

$$h\nu_5 + 1\sigma_g^2\mathbf{1\sigma_u^2}2\sigma_g^2 2\sigma_u^2 3\sigma_g^2\mathbf{1\pi_u^4 1\pi_g^2} \xrightarrow[ionization]{core} 1\sigma_g^2\mathbf{1\sigma_u^1}2\sigma_g^2 2\sigma_u^2 3\sigma_g^2\mathbf{1\pi_u^4 1\pi_g^2} + e_p^- \xrightarrow[ionization]{auto-} 1\sigma_g^2\mathbf{1\sigma_u^2}2\sigma_g^2 2\sigma_u^2 3\sigma_g^2\mathbf{1\pi_u^3 1\pi_g^1} + e_p^- + e_A^-.$$

The lifetimes of core holes are typically from 1 to 100 fs [4], and they are usually shorter than the ones of valence holes.

The aforementioned processes may involve additional shake-up or shake-off transitions, which refer to the transition of an outer electron to an excited state or vacuum concurrently with the departing photoelectron or Auger electron.

2.3 Multi-body fragmentation mechanisms

Relaxation of the electronic structure can involve breaking chemical bonding in a molecule, which cleaves the molecule at the corresponding bond. Specially, Auger processes, as a consequence of ionization or excitation of a core-level electron, have great probability to drive a molecule onto high energy areas on PESs which have a high tendency to dissociate into smaller fragments via various multi-body fragmentation mechanisms. Here we limit the discussion to doubly charged parent molecules after core ionization and normal Auger decay.

From a doubly charged final state, a molecule of light elements may dissociate into a final doubly charged fragment and other neutral co-fragment(s), but these channels turn out to be very minor or even zero according to the research papers included in the thesis. Instead, channels producing two singly charged cations (and other possible neutral co-fragment(s)) predominate, and they can be efficiently investigated by using triple coincidence, photoelectron photo-ion photo-ion coincidence (PEPIPICO) spectroscopy. Next, fragmentation resulting in two singly charged and other possible neutral co-fragment(s) will be surveyed.

Two-body dissociation mechanisms leading into two singly charged fragments are quite simple. In fact, experimental data on the mechanisms is almost self-explanatory. Extracting fragmentation information from experimental data will be discussed in detail in the following chapter.

Three-body dissociation mechanisms are a little more complicated. The typical categories according to the time evolution of the three-body process are:

- **Type IIIa**: *Deferred charge separation*, where charge separation occurs after the ejection of a neutral fragment[1],

$$\{A,B,C\}^{++} \longrightarrow \begin{cases} A \\ \{B,C\}^{++} \xrightarrow[separation]{charge} \begin{cases} \mathbf{B}^{+} \\ \mathbf{C}^{+} \end{cases} \end{cases} \qquad \text{(Type IIIa)}$$

- **Type IIIb**: *Secondary dissociation*, where charge separation occurs prior to the ejection of a neutral fragment,

$$\{A,B,C\}^{++} \xrightarrow[separation]{charge} \begin{cases} \mathbf{A}^{+} \\ \{B,C\}^{+} \longrightarrow \begin{cases} B \\ \mathbf{C}^{+} \end{cases} \end{cases} \qquad \text{(Type IIIb)}$$

- **Type IIIc**: *Concerted dissociation*, where all fragments are released simultaneously,

$$\{A,B,C\}^{++} \xrightarrow[separation]{charge} \begin{cases} A \\ \mathbf{B}^{+} \\ \mathbf{C}^{+} \end{cases} \qquad \text{(Type IIIc)}$$

Four-body dissociation mechanisms can generally have a large variety of different dissociation pathways. Here, we shall constrain examination

[1]The letters of the alphabet in curly braces represent a set of various final fragments. The sets of different dissociation process types are independent, and boldface characters are final charged fragments.

of four-body dissociation mechanisms to a few cases which are not too demanding for studies using the PEPICO technique. The different fragmentation types are listed next; again classified according to the time sequence of fragment release:

- **Type IVa**: Charge separation occurs in the last phase,

$$\{A,B,C,D\}^{++} \longrightarrow \begin{cases} A \\ \{B,C,D\}^{++} \longrightarrow \begin{cases} B \\ \{C,D\}^{++} \xrightarrow[sep.]{charge} \begin{cases} \mathbf{C}^{+} \\ \mathbf{D}^{+} \end{cases} \end{cases} \end{cases}$$

(Type IVa)

- **Type IVb**: A deferred charge separation associated with tertiary dissociation,

$$\{A,B,C,D\}^{++} \longrightarrow \begin{cases} A \\ \{B,C,D\}^{++} \xrightarrow[sep.]{charge} \begin{cases} \mathbf{B}^{+} \\ \{C,D\}^{+} \longrightarrow \begin{cases} C \\ \mathbf{D}^{+} \end{cases} \end{cases} \end{cases}$$

(Type IVb)

- **Type IVc**: A charge separation followed by secondary and tertiary dissociation,

$$\{A,B,C,D\}^{++} \xrightarrow[separation]{charge} \begin{cases} \mathbf{A}^{+} \\ \{B,C,D\}^{+} \longrightarrow \begin{cases} B \\ \{C,D\}^{+} \longrightarrow \begin{cases} C \\ \mathbf{D}^{+} \end{cases} \end{cases} \end{cases}$$

(Type IVc)

- **Type IVd**: Symmetrical charge separation followed by secondary

dissociations,

$$\{A,B,C,D\}^{++} \xrightarrow[separation]{charge} \begin{cases} \{A,B\}^{+} \longrightarrow \begin{cases} A \\ \mathbf{B}^{+} \end{cases} \\ \{C,D\}^{+} \longrightarrow \begin{cases} C \\ \mathbf{D}^{+} \end{cases} \end{cases} \qquad \text{(Type IVd)}$$

These are preliminary schemes describing some of the multi-body fragmentation mechanisms. In the following chapter, we shall discuss *i.a.* how ionic dissociation products are captured and how their fragmentation dynamics can be determined based on experimental data.

Chapter 3

Experimental method

The energy-resolved photoelectron photo-ion coincidence (PEPICO) technique combined with the wide energy spectrum of synchrotron radiation sources provide a powerful means to study photo-fragmentation processes. The tunability of synchrotron radiation gives flexibility in choosing a specific photon energy of interest ranging from infra-red to X-rays [2, 30]. The coincidence technique enables gathering information about changes in the electronic structure and about resulting ionic parent system or dissociated ionic fragments concurrently. Although possible neutral fragments are invisible to the apparatus, the information is sufficient to enable building a good picture of photo-fragmentation processes in most cases.

The principal contribution of the author has been in theoretical modelling and data analysis, rather than in experimental work. Therefore, the goal of this chapter is to present only briefly the main concepts of experimental methods and essential devices used in the research by first introducing measurement related components in Section 3.1. The main part of this chapter comprises data processing methods in Section 3.2.

3.1 Apparatus

Figure 3.1 depicts the general measurement setup of the PEPICO technique. Undulator based monochromated synchrotron radiation interacts

with a target sample in the gase phase. Electrons and ions departed from the target sample are measured in coincidence by using a hemispherical electron analyser and an ion time-of-flight mass spectrometer respectively.

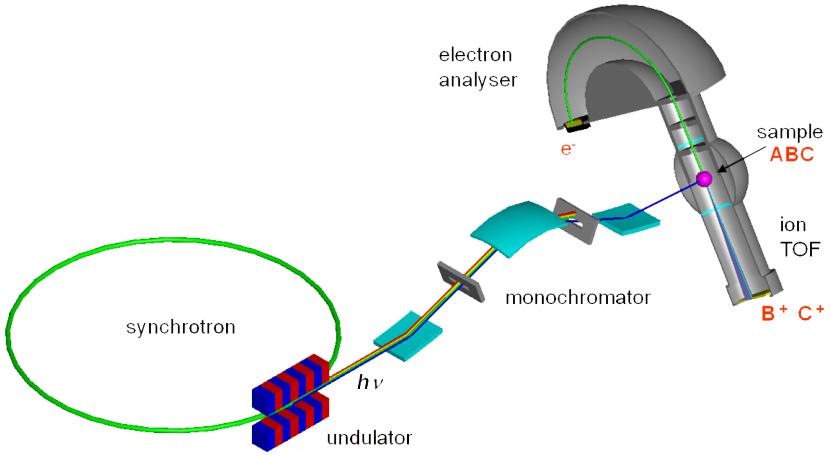

Figure 3.1: PEPICO measurement setup with a synchrotron radiation storage ring as a light source. (Figure from [25])

3.1.1 Electron spectrometer

Apart from low transmission, a dispersive electron spectrometer is an excellent device for studying the electronic structure of a system, since it can be used to probe free electrons posing certain kinetic energy range and to record their energy distribution with high energy resolution. The dispersive hemispherical electron analyser SCIENTA SES-100 [16] has been used as the electron spectrometer in the research included in this thesis.

3.1.2 Time-of-flight mass spectrometer

There are a number of different designs of ion mass spectrometers, optimized for very high mass resolution, sensitivity, velocity mapping *etc.*

The spectrometer used in this work is the well-known Wiley and McLaren time-of-flight (TOF) design [48]. It has the advantage of simple operation, efficiency and quite good mass resolution. In addition to the determination of ion mass-to-charge ratios, the spectrometer also provides data about ion velocities. The axial velocity information can be extracted from the ion flight times, as explained later. Also, the spectrometer is equipped with a position sensitive anode, encoding the radial distance of the hit position from the spectrometer's axis. However, this instalment was not used in the present work.

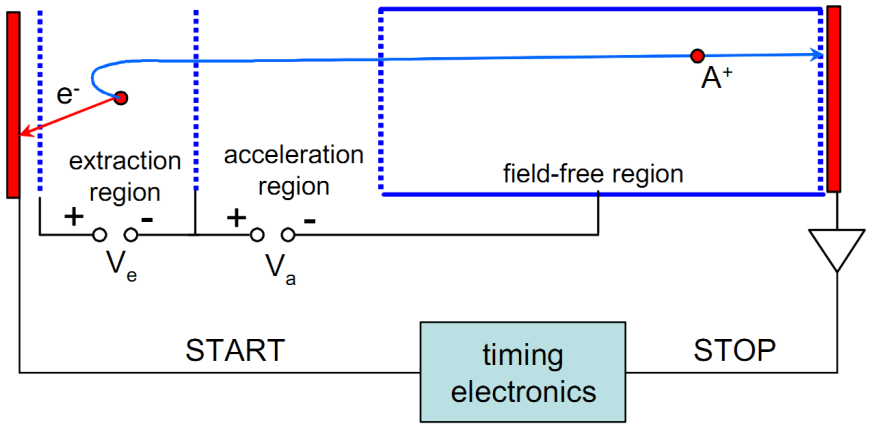

Figure 3.2: Simplified operational picture of a time-of-flight tube. The three principal regions are explained in the text. A simple electron detector on the left (red vertical bar) can be replaced by an electron spectrometer in order to perform PEPICO measurements. (Figure from [25])

The ion TOF spectrometer consists of three regions: extraction region, acceleration region, and field-free region (see Figure 3.2). The mission of the first part, the extraction region, is to direct the initial velocities of ions towards the detector by applying extraction voltage V_e between two grids bordering the region. The timer for flight time measurements is started conventionally by a pulsed excitation voltage source, but in PEPICO technique a cooperative electron detector can start the timer as well. In the acceler-

ation region, the ions are appropriately accelerated to enter the field-free region, in which ions posing different mass-to-charge ratios drift in different time before hitting the ion detector. The flight time and hit positions of the ions are recorded by data acquisition electronics. Flight times of ions can be converted to mass-to-charge ratios for chemical composition determination by either computing values derived directly from parameters of the spectrometer or simply via equation [25]

$$\frac{M}{q} = \left(\frac{T - T_0}{C_0}\right)^2 \tag{3.1}$$

The two calibration parameters T_0 and C_0 are easily obtained by measuring flight times of two known mass-to-charge ratios.

3.1.3 Synchrotron radiation

Synchrotron light source [10] produces bright and tunable radiation which enables the usage of a wide spectrum of photon energies ($10^{-1} - 10^5$ eV) [2, 30] for probing electronic structures of target systems. The radiation is produced by forcing charged particles, usually electrons, to accelerate radially in a storage ring with the help of bending magnets or insertion devices such as undulators and wigglers which contain magnet pairs of alternating polarity for producing very bright radiation. Synchrotron storage ring is connected to experimental stations via straight sections (*i.e.* beamlines). Typically, radiation of specific energy is chosen from a synchrotron radiation spectrum by monochromators before entering an experimental station.

3.1.4 Experimental station

The coincidence measurements in this research were performed at an experimental station which consists of different measuring components such as the hemispherical electron analyser, the Wiley & McLaren TOF spectrometer described earlier and resistively heated oven for evaporating molecules into gas phase. The experimental works included in the thesis were performed by transferring the experimental station to either the FinEst branch

of the beamline I3 of MAX-III [35, 46] or the soft X-ray beamline I411 [5] of MAX-II synchrotron storage ring (Lund, Sweden).

3.2 Data analysis

Depending on the setup of measurements and the study of interest, measured data can be presented in various forms such as in *electron energy, ion mass or coincidence (CIY) or partial (PIY) ion yield spectrum, PEPICO* or *PIPICO map etc.*. The measured data in this work is processed into spectrum and map forms by the help of the macro package [24] implemented in Igor Pro environment. In the following, the main features of data analysis will be presented. We shall begin by discussing how to manage a serious concern in coincidence measurements - *false coincidences*.

3.2.1 False coincidences

A particular disadvantage of coincidence technique is that distinguishing true coincidences from false ones in single events is often simply impossible. Namely, a PEPICO setup is capable of detecting only one electron for every photo-fragmentation event, but multiple events can occur in a short time interval smaller than *dead time* of the ion detector (or simply at the same time on perspective of the ion detector). Therefore, an electron and an ion arriving at their respective detectors in coincidence may not belong to the same photo-fragmentation event.

In practice, false coincidences have to be removed by statistical analysis. The first strategy to deal with the problem is naturally to attempt to keep the rate of ionization events as low as possible, which decreases the probability of several events happening at the same time. Additionally, other special techniques can be adopted, such as using random triggers in addition to electron triggers to detect ions and measure their flight times. In the end, false coincidences can be averagely subtracted from the true coincidences with appropriate analysis procedures [24].

3.2.2 PIPICO map

In order to inspect molecular fragmentation dynamics of doubly charged species that fragment into two or more ions, the acquired flight times of faster ions are plotted along the x axis and the flight times of the slower ions along the y axis to create a 2D TOF correlation map, *i.e.*, a PIPICO map. Patterns on the PIPICO map correspond to the various momentum-correlated cation pairs detected. Depending on kinematics and the orientational distribution of the dissociating molecules, there are patterns with various widths, lengths and tilt angles. Blurring of the patterns occurs due to the presence of neutral ("dark") fragments, reducing the momentum correlation of the ions. The patterns close to the diagonal of equal flight times (concerning ions with the same mass-to-charge ratio) are incomplete, due to deadtime effects that prevented detecting ions arriving less than 30 ns apart, in our study.

3.2.3 PIPICO patterns

Patterns on PIPICO maps not only provide information on chemical composition of detected ions and fragmentation dynamics of a parent molecule, but they also enable computing kinetic energy release (KER) in molecular fragmentation. A KER value reveals the heat in the Coulombic explosion of a charge separation phase or, in other words, how much each *charge separated fragment* inherits kinetic energy from the explosion. The kinetic energy may be delivered to various motions (e.g. vibrational motions) of the fragments or even lead to further fragmentation. KER information can be used to evaluate the theoretically modelled molecular dynamics leading to the related dissociation by contrasting the KER value and the theoretical heat acquired in the simulation.

Fragmentation dynamics and KER values can be determined with good accuracy for two-body dissociation processes. In more complex N-body ($N \geqslant 3$) dissociation processes, where at least one neutral fragment is involved, determination of the KER and fragmentation dynamics must be done approximately. One way to attempt to determine KER and fragmen-

tation dynamics of the complex cases is to approximate by assuming that the energy release is dominant only in the charge separation phase [24]. Distinct phases in multi-body fragmentation mechanisms were introduced in Section 2.3. Here, we discuss how KER and fragmentation dynamics can be derived to a certain extent by inspecting the shapes of the patterns on a PIPICO map.

Let us consider a doubly charged molecule M^{++} dissociating after several phases into the final detected fragments X_i^+ and Y_j^+ (boldface characters in the fragmentation scheme below):

$$M^{++} \longrightarrow \cdots \longrightarrow \begin{cases} P \\ Q^{++} \xrightarrow[separation]{charge} \begin{cases} X_0^+ \longrightarrow \cdots \longrightarrow \begin{cases} x_i \\ \mathbf{X_i^+} \end{cases} \\ Y_0^+ \longrightarrow \cdots \longrightarrow \begin{cases} y_i \\ \mathbf{Y_j^+}, \end{cases} \end{cases} \end{cases}$$

where P & Q^{++} are possible neutral and doubly charged intermediate fragments, respectively, X_0^+ & Y_0^+ are *charge separated fragments*, and x_i, y_i are neutral final fragments. The length of the pattern on a PIPICO map corresponding the square sum of flight time spreads of the final fragments X_i^+ and Y_j^+ is

$$W = \sqrt{(\Delta T_{X_i^+})^2 + (\Delta T_{Y_j^+})^2}. \tag{3.2}$$

The flight time spreads ΔT_* (of X_i^+ or Y_j^+) can be expressed as

$$\Delta T_* = -2\frac{p_*}{\epsilon q} = -2\frac{M_* v_*}{\epsilon q}, \tag{3.3}$$

where p_*, q and M_* are, respectively, the momentum, charge and mass of a certain cationic fragment ejected in an electric field ϵ of the extraction area. Assuming KER is minimal in a dissociation phase without charge separation, velocities of the final fragment and the related charge separated fragment can be approximated as equal, i.e. $v_{X_i^+} \approx v_{X_0^+}$ and $v_{Y_j^+} \approx v_{Y_0^+}$.

Therefore, momentum of the final fragment X_i^+ (or Y_j^+) can be expressed in terms of momentum of the related charge separated intermediate fragment X_0^+ (or Y_0^+):

$$p_{X_i^+} = -\frac{M_{X_i^+}}{M_{X_0^+}} p_{X_0^+} \tag{3.4}$$

$$p_{Y_j^+} = -\frac{M_{Y_j^+}}{M_{Y_0^+}} p_{Y_0^+}. \tag{3.5}$$

Noting also that the momenta of X_0^+ and Y_0^+ are equal but opposite ($p_{X_0^+} = -p_{Y_0^+} = p_0$), the velocity of the final fragment X_i^+ can be expressed in terms of velocity of the charge separated fragment Y_0^+ and *vice versa*:

$$v_{X_i^+} = -\frac{M_{Y_0^+}}{M_{X_0^+}} v_{Y_0^+} \tag{3.6}$$

$$v_{Y_j^+} = -\frac{M_{X_0^+}}{M_{Y_0^+}} v_{X_0^+}. \tag{3.7}$$

Additionally, the length (Equation 3.2) of a pattern on a PIPICO map can be expanded as

$$\begin{aligned} W =& \frac{2}{\epsilon q} \sqrt{\left(-\frac{M_{X_i^+}}{M_{X_0^+}} p_{X_0^+}\right)^2 + \left(-\frac{M_{Y_j^+}}{M_{Y_0^+}} p_{Y_0^+}\right)^2} \\ =& \frac{2p_0}{\epsilon q} \sqrt{\left(\frac{M_{X_i^+}}{M_{X_0^+}}\right)^2 + \left(\frac{M_{Y_j^+}}{M_{Y_0^+}}\right)^2}. \end{aligned} \tag{3.8}$$

As a result, the approximate KER in a charge separation phase is

$$\begin{aligned} E_{KER} =& \left(\frac{1}{2M_{X_0^+}} + \frac{1}{2M_{Y_0^+}}\right) p_0^2 \\ =& \left(\frac{1}{2M_{X_0^+}} + \frac{1}{2M_{Y_0^+}}\right) \frac{1}{4} \frac{(W\epsilon q)^2}{\left(\frac{M_{X_i^+}}{M_{X_0^+}}\right)^2 + \left(\frac{M_{Y_j^+}}{M_{Y_0^+}}\right)^2}. \end{aligned} \tag{3.9}$$

In a special case where cations X_0^+ and Y_0^+ do not dissociate any further ($i = 0 = j$), the formula for KER is simplified to

$$E_{KER} = \left(\frac{1}{2M_{X_0^+}} + \frac{1}{2M_{Y_0^+}} \right) \frac{(W\epsilon q)^2}{8}. \tag{3.10}$$

Now we shall focus on the derivation of fragmentation dynamics based on the slope of the pattern. On a PIPICO map, slower flight times are always plotted against faster flight times, which defines the pattern slope accordingly. Defining the notation so that the final fragment Y_j^+ is heavier than the final fragment X_i^+, the slope of the pattern corresponding to the cation pair is:

$$k = \frac{\Delta T_{Y_j^+}}{\Delta T_{X_i^+}} = \frac{M_{Y_j^+}}{M_{X_i^+}} \frac{v_{Y_j^+}}{v_{X_i^+}}. \tag{3.11}$$

After substituting Equation (3.7) into the equation above and adopting the approximation $v_{X_i^+} \approx v_{X_0^+}$, the slope can be computed by

$$k = \frac{\Delta T_{Y_j^+}}{\Delta T_{X_i^+}} = -\frac{M_{Y_j^+}}{M_{X_i^+}} \frac{M_{X_0^+}}{M_{Y_0^+}}. \tag{3.12}$$

If the final fragment Y_j^+ is lighter than the final fragment X_i^+, the slope definition is reciprocal:

$$k = \frac{\Delta T_{X_i^+}}{\Delta T_{Y_j^+}} = -\frac{M_{X_i^+}}{M_{Y_j^+}} \frac{M_{Y_0^+}}{M_{X_0^+}}. \tag{3.13}$$

Again, in a special case where cations X_0^+ and Y_0^+ stay intact, the slope equation is simplified to

$$k = \frac{\Delta T_{Y_0^+}}{\Delta T_{X_0^+}} = -1 \qquad or \qquad k = \frac{\Delta T_{X_0^+}}{\Delta T_{Y_0^+}} = -1, \quad if\, M_{X_0^+} > M_{Y_0^+}. \tag{3.14}$$

Let us consider a two-body fragmentation process of an unstable dou-

bly charged molecule, where charge is evenly divided between the two fragments. As a result of Coulombic repulsion, the two cationic fragments attain initial velocities in opposite directions. On the PIPICO map, the pattern corresponding to the process is tilted and its slope is $k = -1$, and the KER can be computed by using Equation (3.10).

Charge separation in three-body fragmentation mechanisms involving doubly charged species can arise in three different ways as seen in Section 2.3. *Deferred charge separation process* (Type IIIa) can be approximated to be the aforementioned two-body fragmentation mechanism given that energy release in the neutral fragment's departure is minimal. Thus, the slope is of the corresponding pattern $k \approx -1$, but the pattern can be rather wide. Likewise, the KER can be estimated by using Equation (3.10). In *concerted dissociation* (Type IIIc), patterns do not have clearly defined slopes and therefore the respective momentum correlation is vague. Patterns corresponding to *secondary dissociation* (Type IIIb) cases are rather easily analysed but still not trivial. If cation A^+ (ejected in the primary phase) is heavier than cation C^+ (ejected in the secondary phase) and energy release is minimal in the secondary phase, the slope is approximately (referring to Equations (3.12 or 3.13)):

$$k = \frac{\Delta T_{A^+}}{\Delta T_{C^+}} \approx -\frac{M_{\{B,C\}^+}}{M_{C^+}}, \tag{3.15}$$

whereas the slope, if cation A^+ is lighter than cation C^+, is approximately:

$$k = \frac{\Delta T_{C^+}}{\Delta T_{A^+}} \approx -\frac{M_{C^+}}{M_{\{B,C\}^+}}. \tag{3.16}$$

The approximate KER in a *secondary charge separation* (Type IIIb) case is

$$E_{KER} = \left(\frac{1}{2M_{A^+}} + \frac{1}{2M_{\{B,C\}^+}}\right) \frac{1}{4} \frac{(W\epsilon q)^2}{1 + \left(\frac{M_{C^+}}{M_{\{B,C\}^+}}\right)^2}. \tag{3.17}$$

For most cases, patterns corresponding to four-body or more complex

fragmentation are naturally more difficult to derive than in three-body fragmentation. In Section 2.3, we introduced four fragmentation pathways which do not require much effort to be derived from the patterns in four-body dissociation processes involving doubly charged species. Here, applying Equations (3.12, 3.13 and 3.9) one can estimate respective pattern slopes and KERs for interpreting data on a PIPICO map:

- Type IVa, last step charge separation

$$k = \frac{\Delta T_{C^+}}{\Delta T_{D^+}} \approx -1, \qquad if\, M_{C^+} > M_{D^+} \tag{3.18}$$

$$k = \frac{\Delta T_{D^+}}{\Delta T_{C^+}} \approx -1 \qquad if\, M_{D^+} < M_{C^+}. \tag{3.19}$$

$$E_{KER} = \left(\frac{1}{2M_{C^+}} + \frac{1}{2M_D^+}\right)\frac{(W\epsilon q)^2}{8}. \tag{3.20}$$

- Type IVb, deferred charge separation associated with tertiary dissociation

$$k = \frac{\Delta T_{B^+}}{\Delta T_{D^+}} \approx -\frac{M_{\{C,D\}^+}}{M_{D^+}}, \qquad if\, M_{B^+} > M_{D^+} \tag{3.21}$$

$$k = \frac{\Delta T_{D^+}}{\Delta T_{B^+}} \approx -\frac{M_{D^+}}{M_{\{C,D\}^+}} \qquad if\, M_{B^+} < M_{D^+}. \tag{3.22}$$

$$E_{KER} = \left(\frac{1}{2M_{B^+}} + \frac{1}{2M_{\{C,D\}^+}}\right)\frac{1}{4}\frac{(W\epsilon q)^2}{1 + \left(\frac{M_{D^+}}{M_{\{C,D\}^+}}\right)^2}. \tag{3.23}$$

- Type IVc, charge separation followed by secondary and tertiary dissociation

$$k = \frac{\Delta T_{A^+}}{\Delta T_{D^+}} \approx -\frac{M_{\{B,C,D\}^+}}{M_{D^+}}, \qquad if\, M_{A^+} > M_{D^+} \tag{3.24}$$

$$k = \frac{\Delta T_{D^+}}{\Delta T_{A^+}} \approx -\frac{M_{D^+}}{M_{\{B,C,D\}^+}} \qquad if\, M_{A^+} < M_{D^+}. \tag{3.25}$$

$$E_{KER} = \left(\frac{1}{2M_{A^+}} + \frac{1}{2M_{\{B,C,D\}^+}}\right) \frac{1}{4} \frac{(W\epsilon q)^2}{1 + \left(\frac{M_{D^+}}{M_{\{B,C,D\}^+}}\right)^2}. \tag{3.26}$$

- Type IVd, symmetrical charge separation followed by secondary dissociations

$$k = \frac{\Delta T_{B^+}}{\Delta T_{D^+}} \approx -\frac{M_{B^+}}{M_{D^+}} \frac{M_{\{C,D\}^+}}{M_{\{A,B\}^+}}, \qquad if\, M_{B^+} > M_{D^+} \tag{3.27}$$

$$k = \frac{\Delta T_{D^+}}{\Delta T_{B^+}} \approx -\frac{M_{D^+}}{M_{B^+}} \frac{M_{\{A,B\}^+}}{M_{\{C,D\}^+}} \qquad if\, M_{B^+} < M_{D^+}. \tag{3.28}$$

$$E_{KER} = \left(\frac{1}{2M_{\{A,B\}^+}} + \frac{1}{2M_{\{C,D\}^+}}\right) \frac{1}{4} \frac{(W\epsilon q)^2}{\left(\frac{M_{B^+}}{M_{\{A,B\}^+}}\right)^2 + \left(\frac{M_{D^+}}{M_{\{C,D\}^+}}\right)^2}. \tag{3.29}$$

The approximations aid in interpreting fragmentation dynamics from experimental data. However, the approximations deteriorate as the number of steps of a fragmentation process increases. Moreover, PIPICO pattern shapes are obscure in several cases and hence detailed information on the corresponding fragmentation dynamics is lost. The incomplete information can be overcome by *ab initio* calculations. In the following chapter, we will review various *ab initio* methods comprising different ways to study electronic structure and nuclear motion theoretically.

Chapter 4

Ab initio methods

The PEPICO technique combined with synchrotron radiation offers a sound way to probe photo-fragmentation events of small molecules, but the output data is limited to time-of-flights of created ions and kinetic/binding energies of ejected electrons. Combining the experimental technique with *ab initio* methods provides further insight into the electronic structure and nuclear motions of the system of interest.

This chapter overviews the *ab initio* methods implemented in the computer software packages which were used in the research. The Hartree-Fock (HF) method will be presented first in Section 4.1. In what follows, the methods based on density functional theory (DFT) will be briefly recapitulated starting from the DFT itself in Section 4.2, then time-dependent density functional theory (TDDFT) will be presented in Section 4.3. The end of this chapter is reserved for *ab initio* molecular dynamic methods (MD): Time-dependent density functional theory -based Ehrenfest molecular dynamics (TDDFT-EMD) in Section 4.4, Born-Oppenheimer molecular dynamics (BO MD) in Section 4.5 and Car-Parrinello molecular dynamics (CP MD) in Section 4.6.

4.1 Hartree-Fock method

The Hartree-Fock method comprises the solutions of the electronic Schrödinger equation for a single electron moving in a mean potential field affected by the remaining electrons and the nuclei of a given molecular system [33]. Analysis of the solutions of the electronic Schrödinger equation provides understanding of the properties and the internal interactions of the stationary system within the constraints of Born-Oppenheimer approximation [6]. The traditional way to proceed with the derivation of the HF equations is to prospect the time-independent non-relativistic Schrödinger equation

$$\mathbf{H}\Psi(\mathbf{r},\mathbf{s},\mathbf{R}) = \mathbf{E}\Psi(\mathbf{r},\mathbf{s},\mathbf{R}), \tag{4.1}$$

where $\mathbf{H}$ is the total energy operator, $\mathbf{E}$ the energy, and $\Psi(\mathbf{r},\mathbf{s},\mathbf{R})$ an unknown total wave function of a given system. The total wave function depends on positions of N nuclei $\mathbf{R} = (R_1, R_2, .., R_N)$, positions $\mathbf{r} = (r_1, r_2, .., r_n)$ and spin $\mathbf{s} = (s_1, s_2, .., s_n)$ of n electrons. In the absence of external fields, the Hamiltonian $\mathbf{H}$ describing the motions of the particles in a molecular system (in atomic units) is [8]

$$\mathbf{H} = -\frac{1}{2}\sum_{i}^{n}\nabla_i^2 - \frac{1}{2M_I}\sum_{I}^{N}\nabla_I^2 - \sum_{i<j}^{n}\frac{1}{r_{ij}} + \sum_{i}^{n}\sum_{I}^{N}\frac{Z_I}{r_{iI}} + \sum_{I<J}^{N}\frac{Z_I Z_J}{r_{IJ}}, \tag{4.2}$$

where the first two terms contribute to kinetic energies of n electrons and N nuclei in the system and the last three terms describe the Coulomb pair interactions between electron-electron, electron-nucleus and nucleus-nucleus respectively. In fact, the motion of every single particle in the system is correlated to the one of the other particles and describing such a complicated system is an extremely formidable task. With this in mind, BO approximation simplifies the correlation by separation motions of the electrons and the nuclei, since a proton is about 1800 times heavier than an electron which suggests that motions of the two particle types occur in different time scales. In this sense, electrons can be considered to move in the Coulomb field of fixed nuclei. The total energy operator is therefore

simplified to

$$\mathbf{H^{BO}} = -\frac{1}{2}\sum_{i}^{n}\nabla_i^2 - \sum_{i<j}^{n}\frac{1}{r_{ij}} + \sum_{i}^{n}\sum_{I}^{N}\frac{Z_I}{r_{iI}} + \sum_{I<J}^{N}\frac{Z_I Z_J}{r_{IJ}} \tag{4.3}$$

$$= \mathbf{H^e} + \sum_{I<J}^{N}\frac{Z_I Z_J}{r_{IJ}}, \tag{4.4}$$

where the kinetic energy term of the nuclei is omitted and the first three terms on the r.h.s. of Equation (4.3) are conventionally denoted to the electronic Hamiltonian $\mathbf{H^e}$. In addition to the reduction of the total energy operator, decoupling in the BO approximation also lets the total wave function separate into electronic $\Psi^e(\mathbf{r},\mathbf{s};\mathbf{R})$ and nuclear $\Psi^{nuc}(\mathbf{R})$ wave functions: $\Psi(\mathbf{r},\mathbf{s},\mathbf{R}) = \Psi^e(\mathbf{r},\mathbf{s};\mathbf{R})\Psi^{nuc}(\mathbf{R})$. The n-electron wave function $\Psi^e(\mathbf{r},\mathbf{s};\mathbf{R})$ is a regular function constructed from one-electron spin orbitals $\chi_i(r_i,s_i;\mathbf{R})$[1]. Within the framework of Born-Oppenheimer approximation, the wave function Ψ^e depends explicitly on the coordinates of any one of the electrons but parametrically on the coordinates of the nuclei. In other words, the wave function Ψ^e describes the distribution of all the electrons in the presence of the potential field affected by the fixed nuclei. To ensure the Pauli principle and the indistinguishability of electrons (of a closed-shell system), in the Hartree-Fock method the spin orbitals are arranged in a Slater determinant [41]

$$\Psi^e(\mathbf{r,s;R}) = \frac{1}{\sqrt{n!}}\begin{vmatrix} \psi_1(r_1;\mathbf{R})\alpha(s_1) & \psi_1(r_1;\mathbf{R})\beta(s_1) & \cdots & \psi_{\frac{n}{2}}(r_1;\mathbf{R})\beta(s_1) \\ \psi_1(r_2;\mathbf{R})\alpha(s_2) & \psi_1(r_2;\mathbf{R})\beta(s_2) & \cdots & \psi_{\frac{n}{2}}(r_2;\mathbf{R})\alpha(s_2) \\ \vdots & \vdots & \ddots & \vdots \\ \psi_1(r_n;\mathbf{R})\alpha(s_n) & \psi_1(r_n;\mathbf{R})\beta(s_n) & \cdots & \psi_{\frac{n}{2}}(r_n;\mathbf{R})\alpha(s_n) \end{vmatrix}$$

From algebraic manipulation upon the expectation value of the electronic Hamiltonian $\mathbf{H^e}$ in the basis of the determinantal electronic function

[1] One-electron spin orbitals $\chi_i(r_i,s_i;\mathbf{R})$ can also be written in separable forms consisting of spatial and spin functions: $\chi_i(r_i,s_i;\mathbf{R}) = \psi_i(r_i;\mathbf{R})\alpha(s_i)$ or $\psi_i(r_i;\mathbf{R})\beta(s_i)$.

$\Psi^e(\mathbf{r},\mathbf{s};\mathbf{R})$ one can derive HF integro-differential equations [27, 33]

$$\begin{aligned} F_i\,\chi_i(a) = \Bigg\{ & -\frac{1}{2}\nabla_a^2 + \sum_I^N \frac{Z_I}{r_{aI}} \\ & + \sum_j^{\frac{n}{2}} [2\int \chi_j(b)\chi_j(b)\frac{1}{r_{ab}}\chi_i(a)d\tau_b \\ & - \int \chi_j(b)\chi_i(b)\frac{1}{r_{ab}}\chi_j(a)d\tau_b)] \Bigg\}\,\chi_i(a) \\ & = \{H^{core} + \sum_j^{\frac{n}{2}}[2J_j - K_j]\}\,\chi_i(a) \qquad = E_i\,\chi_i(a), \end{aligned} \tag{4.5}$$

where the two terms on the r.h.s of the first row are called core Hamiltonian, whereas the integrals in the second and the third row are Coulomb and exchange operator respectively. Together they are called the Fock operator. The molecular spin orbital $\chi_i(a)$ in Equation (4.5) corresponds to electron a and $\chi_i(b)$ to electron b.

Up to this point, the total energy (the Fock plus the Coulomb term of nucleus-nucleus interactions) operator and the way to construct the wave function are presented. The question remains how to solve the energies and the corresponding molecular spin orbitals from the HF integro-differential equations (4.5) while the Fock operator is readily built from 'unknown' spin orbitals. To this aim, Roothaan and Hall independently invented to present the spatial orbitals $\psi_i(r_i;\mathbf{R})$ as linear combinations of familiar orthogonal atomic wave functions or *basis functions*:

$$\psi_i(r_i;\mathbf{R}) \quad = \quad \sum_{\nu=1}^{B} c_{\nu i}\phi_\nu \tag{4.6}$$

where the associated coefficients $c_{\nu i}$ are to be optimized to correspond well the given spatial orbital by using the variational theorem[1] upon the Hartree-

[1]The HF theory is built on the variational theorem

$$\frac{\int \psi\,\mathbf{H}\psi d\tau}{\int \psi\,\psi d\tau} = E \geq E_0.$$

Fock integro-differential equations.

As a result, the HF equations can be represented in the so-called Roothaan-Hall matrix equation [13, 37]:

$$\sum_{\nu=1}^{B} c_{\nu i} \int d\tau_a \phi_\mu(a) F_i \phi_\nu(a) = E_i \sum_{\nu=1}^{B} c_{\nu i} \int d\tau_a \phi_\mu(a) \phi_\nu(a)$$
$$\sum_{\nu=1}^{B} c_{\nu i} F_{\mu\nu} = E_i \sum_{\nu=1}^{B} c_{\nu i} S_{\mu\nu}, \tag{4.7}$$

which leads to the secular determinant [42]

$$\begin{vmatrix} F_{11} - ES_{11} & F_{12} - ES_{12} & \cdots & F_{1A} - ES_{1A} \\ F_{21} - ES_{21} & F_{22} - ES_{22} & \cdots & F_{2A} - ES_{2A} \\ \vdots & \vdots & \ddots & \vdots \\ F_{A1} - ES_{A1} & F_{A2} - ES_{A2} & \cdots & F_{AA} - ES_{AA} \end{vmatrix} = 0. \tag{4.8}$$

The Fock matrix elements in the Roothaan-Hall equation (4.7) are:

$$F_{\mu\nu} = \int d\tau_a \phi_\mu(a) H^{core} \phi_\nu(a) + \sum_{j}^{\frac{n}{2}} \int d\tau_a \phi_\mu(a) [2J_j - K_j] \phi_\nu(a), \tag{4.9}$$

or in the generally used notation [27, 33, 42]:

$$F_{\mu\nu} = \langle \mu | - \frac{1}{2} \nabla^2 | \nu \rangle - \sum_{I}^{N} Z_I \left\langle \mu \right| - \frac{1}{r_{aI}} \left| \nu \right\rangle + \sum_{\lambda\sigma}^{B} P_{\lambda\sigma} [(\mu\nu|\lambda\sigma) - (\mu\lambda|\nu\sigma)], \tag{4.10}$$

where the operators are expressed in atomic units and the basis functions

The ansatz provides a powerful way to judge the quality of the trial wave function by stating that the energy E cannot be below the exact ground-state energy E_0 by any used arbitrary trial wave function and the exact energy can be achieved only by using the correct wave function. For this reason, the better basis functions are adopted, the closer the exact ground-state energy is attained. However, in the basis of the true wave function the expectation value of the Fock operator for a given system can be lowest at the *Hartree-Fock limit*, i.e. E_{cor} higher than the exact energy ($E_{exact} = E_{HF} + E_{cor}$), due to the price of averaging the electron-electron correlation interactions [8].

are abbreviated by their indexes. In addition, the density matrix

$$P_{\lambda\sigma} = 2\sum_{i}^{\frac{n}{2}} c_{\lambda i} c_{\sigma i} \tag{4.11}$$

and the four-index $(\mu\nu|\lambda\sigma)$ comprising two-electron integrals as well as the two-index $\langle\mu| O |\nu\rangle$ comprising one-electron integrals are introduced.

Thus, the HF self-consistent field method is an iterative method for solving the energies and corresponding wave functions, in which the Roothaan-Hall matrix form facilitates an elegant way to retrieve the solutions by adopting matrix algebra. Briefly, the HF self-consistent field (SCF) strategy proceeds by choosing a trial wave function to build the Fock operator for solving a new wave function and the corresponding energy. The new wave function then replaces the old wave function in constructing the new Fock operator for the next cycle, and the procedure continues through cycles until the difference between the new and the old wave function is small enough. As a result, single-point energy and other properties of a fixed molecular geometry are given. However, nowadays quantum chemistry computational software also features an option to seek stationary points on the BO PES of a given system. Scheme 4.1 illustrates the HF-SCF procedure [8]:

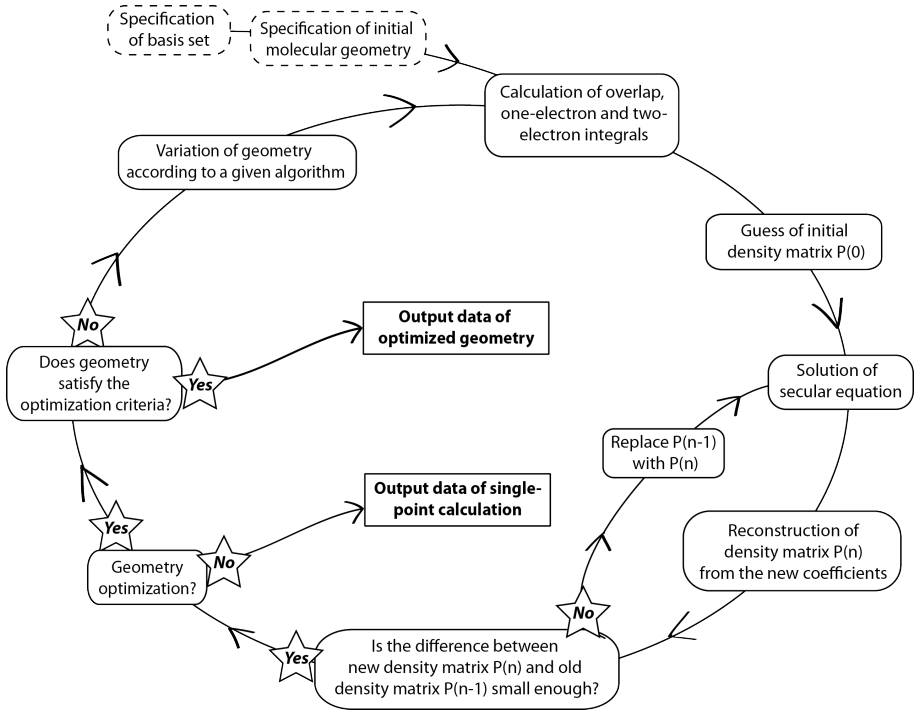

Figure 4.1: Hartree-Fock self-consistent field procedure.

4.2 Density functional theory

The previous section gave us a glimpse of how complicated the HF-SCF method is. Especially, computing the energy of a given system involves tackling (3+1)n coordinate variables of a n-electron system, which becomes computationally unfeasible if the size of the system grows too large. Density functional theory (DFT) is in principle an exact theory for computing quantum mechanical systems based on electron density $\rho(r)$ depending on only three spatial variables ($r = (x, y, z)$). The total energy in DFT is expressed as a unique functional of overall electronic density

$$E = E[\rho(r)]. \tag{4.12}$$

The mainstays of the modern DFT are undoubtedly the two theorems of Hohenberg & Kohn [15] and the Kohn-Sham (KS) formulation [20] from the mid-1960s. The first Hohenberg-Kohn (HK) theorem proved that the electron density of a system determines uniquely its ground-state energy and other quantum mechanical properties. The second HK theorem is based on the variational principle which states that the ground-state energy functional $E_0[\rho]$ is built from the true ground-state density ρ_0 if and only if the functional provides the lowest energy. The theorems do not, however, specify a means to predict the electron density and to form the functional $E[\rho]$ explicitly. To this aim, Kohn and Sham formulated from a non-interacting reference system an electron density reminiscent of the electron density of the real system, in which information is attempted to be computed as accurately as possible and the small correction to the total energy is compensated by an approximate functional [8]:

$$E[\rho(r)] = T_e^{non-int}[\rho(r)] + V_{ee}[\rho(r)] + V_{ne}[\rho(r)] + E_{XC}[\rho(r)]. \tag{4.13}$$

The first three terms on the r.h.s of Equation (4.13) describe, in order, the kinetic energy of non-interacting electrons, the classical electron-electron interaction and the nucleus-electron interaction. The approximate exchange-

correlation functional

$$E_{XC}[\rho(r)] = \Delta T_e[\rho(r)] + \Delta V_{ee}[\rho(r)] \tag{4.14}$$

includes not only quantum-mechanical contributions (self-interaction correction, exchange and correlation) in the potential energy, but also comprises the correction for the kinetic energy of electrons to correspond the true electronic kinetic energy contribution of the real system.

The full KS expression for the total energy functional of a n-electron system is:

$$\begin{aligned} E[\rho(r)] = &\sum_{i}^{n} \int \psi_i(r)(-\frac{\nabla^2}{2})\psi_i(r)dr + \frac{1}{2}\int\int \frac{\rho(r)\rho(r')}{|r-r'|}dr\,dr' \\ &- \sum_{I}^{N} \int \frac{Z_I}{|r-R_I|}\rho(r)dr + E_{XC}[\rho(r)], \end{aligned} \tag{4.15}$$

where electron density ρ is built from the sum of the absolute square of a set of one-electron orthonormal orbitals

$$\rho = \sum_{i}^{n} |\psi_i|^2. \tag{4.16}$$

Now variation of the energy functional under the constraint $< \psi_i|\psi_j >= \delta_{ij}$ leads to the eigenvalue equations [34]:

$$h_i^{KS}\psi_i = E_i\psi_i, \tag{4.17}$$

where the KS one-electron operator is

$$h_i^{KS} = -\frac{1}{2}\nabla^2 - \sum_{I}^{N} \frac{Z_I}{|r_i - R_I|} + \int \frac{\rho(r)}{|r-r'|}dr' + \frac{\delta E_{XC}}{\delta\rho}. \tag{4.18}$$

Note that the last three terms already depend on the density (built from the orbitals), but the goal is to use the operator h_i^{KS} to solve the KS orbitals and thus the density. Therefore, the KS one-electron equations have to

be solved iteratively similarly as in the Hartree-Fock self-consistent field procedure. That is to say, the trial KS orbitals built from a set of basis functions weighted by their separate coefficients

$$\psi_i = \sum_{i}^{B} c_{\nu i}\phi_\nu \tag{4.19}$$

is to be improved by optimizing the coefficients $c_{\mu i}$ via solution of a secular equation analogous to the one in the HF-SCF method. The difference is that the matrix elements $F_{\mu\nu}$ in the HF method are now switched to matrix elements $K_{\mu\nu}$:

$$K_{\mu\nu} = \langle\phi_\mu| - \frac{1}{2}\nabla^2 - \sum_{I}^{N}\frac{Z_I}{|r-R_I|} + \int\frac{\rho(r)}{|r-r'|}dr' + \frac{\delta E_{XC}}{\delta\rho}\,|\phi_\nu\rangle\,. \tag{4.20}$$

The following self-consistence scheme illustrates the iterative procedure for solving the KS equations [8]:

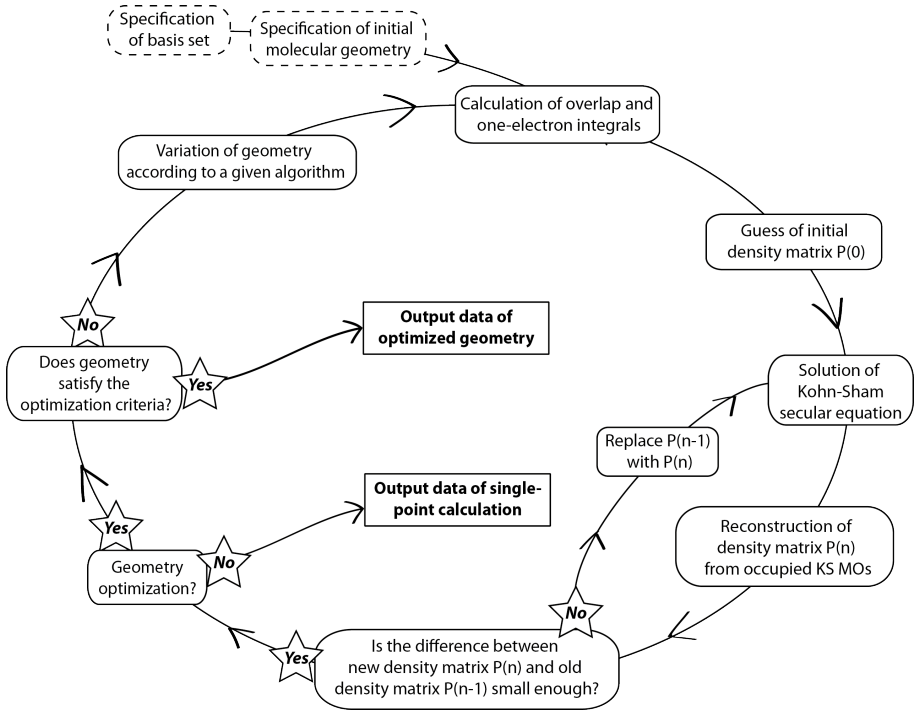

Figure 4.2: Kohn-Sham self-consistent field procedure

4.3 Time-dependent density functional theory

The central idea in the Kohn-Sham formalism of using the electron density of a fictitious system to describe the one of the real system sounds odd, but the theory has rendered successful results in many scientific articles in the recent decades. Yet, the comprehension of the internal dynamics of electronic structures necessitates an extension of DFT to time-dependent density functional theory, which facilitates studying e.g. excited-state properties and other time-dependent phenomena of a system.

TDDFT is based on a one-to-one correspondence between time-dependent potentials $v_{ext}(r,t)$ and time dependent densities $\rho(r,t)$ for a given initial state, which is proved by Runge and Gross [38]. Analogously to the ground-state DFT, Runge-Gross theorem builds the platform for the modern TDDFT on a time-dependent electron density, which can be retrieved by using an auxiliary density of a non-interacting system as the true density to build the functionals for the real system. Thus, the information of all observables of a system is posed by time-dependent density

$$\rho(r,t) = \sum_{j}^{n} |\psi_j(r,t)|^2. \tag{4.21}$$

Time-dependent KS equations are defined as [31]:

$$\imath \frac{\partial \phi_j(r,t)}{\partial t} = \left[-\frac{\nabla^2}{2} + v_{KS}[\rho](r,t) \right] \phi_j(r,t). \tag{4.22}$$

The major contribution of kinetic energy to the real system comes from evaluating the one of the auxiliary non-interacting system, but the correction and the rest of the terms are included in the KS potential

$$v_{KS}[\rho;\Phi_0](r,t) = v_{ext}[\rho;\Psi_0](r,t) + \int d^3r' \frac{\rho(r',t)}{|r-r'|} + v_{XC}[\rho;\Psi_0,\Phi_0](r,t), \tag{4.23}$$

where the v_{ext} term is the external potential term and the second term on the r.h.s of Equation (4.23) is the time dependent Hartree potential,

analogous to the time-independent interaction of classical electronic charge distributions in the ground-state DFT. The extremely complex exchange-correlation potential $v_{XC}[\rho; \Psi_0, \Phi_0](r,t)$ is functional of the KS initial state Φ_0, the initial interaction state Ψ_0 and the density $\rho(r,t)$.

The time-independent KS wave functions ϕ_j and the density $\rho(r,t)$ in the general formulation of the KS equations 4.22 can be solved via various approaches. In CPMD code [45] used in the work, the KS orbitals are propagated in the time propagation scheme

$$\phi_j(t) = U(t,t_0)\phi_j(t_0) \qquad j = 1, ..., n \tag{4.24}$$

where the linear operator $U(t,t_0)$ obeys the Schrödinger-like equation:

$$\imath \frac{dU(t,t_0)}{dt} = H_{KS}(t)U(t,t_0). \tag{4.25}$$

Equation (4.25) can be written in an integral form [31]:

$$U(t,t_0) = \hat{1} - \imath \int_{t_0}^{t} d\tau H(\tau) t(\tau, t_0) \tag{4.26}$$

which can then be formulated, via expansion into a Dyson's series and assuming the Hamiltonian commutes itself at different times, further to

$$U(t,t_0) \simeq \exp\{\imath \int_{t_0}^{t} d\tau H(\tau)\}. \tag{4.27}$$

In practice, the linear operator is divided into smaller time intervals:

$$U(t,t_0) = \prod_{i=0}^{N-1} U(t_i + \Delta t_i, t_i), \tag{4.28}$$

where $t_0 = 0$, $t_{i+1} = t_i + \Delta t_i$ and $t_i = t$. Therefore, the set of equations (4.24) becomes

$$\phi_j(t+\Delta t) = U(t+\Delta t, t)\phi_j(t) = \exp\{\imath \int_{t}^{t+\Delta t} d\tau H(\tau)\}\phi_j(t) \tag{4.29}$$

The time-dependent KS orbitals and the related density are propagated in terms of the linear operator based on the implicit midpoint rule (Crank-Nicholson, CN) method:

$$U_{CN}(t+\Delta t) = \frac{\hat{1} - \frac{\imath}{2}\Delta H_{KS}(t+\Delta t/2)}{\hat{1} + \frac{\imath}{2}\Delta H_{KS}(t+\Delta t/2)} \tag{4.30}$$

combined with a two-step Runge-Kutta scheme [45]. A detailed description of the solution strategy can be reviewed e.g. in the Ph.D. thesis of P. López-Tarifa [29].

4.4 Time-dependent density functional theory - based Ehrenfest molecular dynamics

Ehrenfest molecular dynamics (EMD) is a mixed quantum-classical method describing motions of a system, in which the nuclei are treated as classical point particles but the electronic degrees of freedom are allowed to evolve quantum mechanically. The EMD is a result of distinct works of various authors but it is named after Paul Ehrenfest who was the first to propose the question of how quantum mechanics can be adopted to compute Newtonian classical dynamics.

Following the reformulation of Marx [32], the derivation of EMD may begin by writing out the time-dependent Schrödinger's equation:

$$\imath\hbar\frac{\partial\Phi(\mathbf{r},\mathbf{R},t)}{\partial t} = \mathbf{H}\Phi(\mathbf{r},\mathbf{R},t), \tag{4.31}$$

where the many-body wave function $\Phi(\mathbf{r},\mathbf{R},t)$ depends on time t, coordinates of the electrons $\mathbf{r} = (r_1, r_2, .., r_n)$ and nuclei $\mathbf{R} = (R_1, R_2, .., R_N)$. The Hamiltonian $\mathbf{H}$ of the entire system is defined as Equation (4.2) in

Section 4.1, but here it is presented in the SI units

$$\begin{aligned}\mathbf{H} =& -\frac{\hbar^2}{2M_I}\sum_{I}^{N}\nabla_I^2 \\ & -\frac{\hbar^2}{2m_e}\sum_{i}^{n}\nabla_i^2 - \sum_{i<j}^{n}\frac{e^2}{4\pi\epsilon_0 r_{ij}} + \sum_{i}^{n}\sum_{I}^{N}\frac{Z_I e^2}{4\pi\epsilon_0 r_{iI}} + \sum_{I<J}^{N}\frac{Z_I Z_J e^2}{4\pi\epsilon_0 r_{IJ}} \\ \mathbf{H} =& E_{kin}(\mathbf{R}) + H_r(\mathbf{r},\mathbf{R}) \end{aligned} \tag{4.32}$$

to clarify derivation classical dynamics starting from quantum mechanics. The next essential step is to separate the time-dependent wave function into functions of fast (electronic) motions and slow (nuclei) motions:

$$\Phi(\mathbf{r},\mathbf{R},t) = \Psi(\mathbf{r},t)\Omega(\mathbf{R},t)\exp\left[\frac{\imath}{\hbar}\int_{t_0}^{t}\tilde{E}_r(\tau)d\tau\right]. \tag{4.33}$$

The electronic and the nuclear wave functions, $\Psi(\mathbf{r},t)$ and $\Omega(\mathbf{R},t)$, are normalized at every instant of time with respect to integration of $\mathbf{r}$ and $\mathbf{R}$ respectively. The phase factor in Equation (4.33) is defined as:

$$\tilde{E}_r(t) = \int d\mathbf{r}d\mathbf{R}\Psi^*(\mathbf{r},t)\Omega^*(\mathbf{R},t)H_r\Psi(\mathbf{r},t)\Omega(\mathbf{R},t) \tag{4.34}$$

After substituting the separated wave function $\Phi(\mathbf{r},\mathbf{R},t)$ (Equation (4.33)) in the time-dependent Schrödinger's equation (4.31), multiplying from the left by $\Psi^*(\mathbf{r},t)$ and integrating over $\mathbf{r}$ leads to an effective Schrödinger equation for the nuclei :

$$\imath\hbar\frac{\partial\Omega(\mathbf{R},t)}{\partial t} = \left\{-\frac{\hbar^2}{2M_I}\sum_{I}\nabla_I^2 + \int d\mathbf{r}\Psi^*(\mathbf{r},t)H_r(\mathbf{r},\mathbf{R})\Psi(\mathbf{r},t)\right\}\Omega(\mathbf{R},t) \tag{4.35}$$

Similar algebra with multiplying from the left by $\Omega^*(\mathbf{R},t)$ and integrating over $\mathbf{R}$ leads to an effective Schrödinger equation for the electronic degrees

of freedom:

$$\imath\hbar\frac{\partial\Psi(\mathbf{r},t)}{\partial t}=\left\{-\frac{\hbar^2}{2m_e}\sum_i\nabla_i^2+\int d\mathbf{R}\Omega^*(\mathbf{R},t)V_C(\mathbf{r},\mathbf{R})\Omega(\mathbf{R},t)\right\}\Psi(\mathbf{r},t), \tag{4.36}$$

where the potential $V_C(\mathbf{r},\mathbf{R})$ comprises three Coulomb interaction types of the electrons and nuclei. Equations (4.35) & (4.36) define the mean-field time-dependent self-consistent method describing quantum mechanically the motions of the nuclei in the average field of the electrons and *vice versa*. By the virtue of Ehrenfest approximation, the motions of the slow particles are described classically by adopting Newtonian dynamics. To this aim, the nuclear wave function $\Omega(\mathbf{R},t)$ is rewritten in terms of an amplitude factor A and a phase S:

$$\Omega(\mathbf{R},t)=A(\mathbf{R},t)\exp\left[\frac{\imath}{\hbar}S(\mathbf{R},t)\right]. \tag{4.37}$$

With the new representation of the nuclear wave function, Equation (4.35) becomes

$$\frac{\partial A}{\partial t}+\frac{1}{M_I}\sum_I(\nabla_I A)(\nabla_I S)+\frac{1}{2M_I}\sum_I A(\nabla_I^2 S)=0 \tag{4.38}$$

$$\frac{\partial S}{\partial t}+\frac{1}{2M_I}\sum_I(\nabla_I S)^2+\int d\mathbf{r}\Psi^*H_r\Psi=\frac{\hbar^2}{2M_I}\frac{\sum_I(\nabla_I^2 A)}{A} \tag{4.39}$$

after the separation of the real and imaginary terms. At the classical limit where the reduced Plank constant $\hbar$ is approximated to zero, the r.h.s of Equation (4.39) vanishes. Thus, Equation (4.39) is simplified to

$$\frac{\partial S}{\partial t}+\frac{1}{2M_I}\sum_I(\nabla_I S)^2+\int d\mathbf{r}\Psi^*H_r\Psi=0, \tag{4.40}$$

which is equivalent to Hamilton-Jacobi formulation in classical mechanics:

$$\frac{\partial S}{\partial t}+T(P_I)+V(R_I)=0. \tag{4.41}$$

By using the connecting transformation $P_I = \nabla_I S$ and presuming incompressible fluid[1], Equation (4.40) takes form:

$$\begin{aligned} \frac{\partial P_I}{\partial t} &= -\nabla_I \int d\mathbf{r}\Psi^* H_r \Psi \\ M_I \frac{\partial^2 R_I}{\partial t^2} = F_I &= -\nabla_I \int d\mathbf{r}\Psi^* H_r \Psi \end{aligned} \tag{4.42}$$

Applying the Hellman-Feynman theorem on the gradient part in Equation (4.42) the forces on the nuclei can be related to the expectation values of the gradients of the Hamiltonian H_r:

$$M_I \frac{\partial^2 R_I}{\partial t^2} = -\int d\mathbf{r}\Psi^* \nabla_I H_r \Psi, \tag{4.43}$$

The locations and velocities of the nuclei can computed by integrating the nuclear forces over R by e.g. Verlet algorithm [47].

In time-dependent DFT formalism, the average field generated by electrons is described by time-dependent density (instead of wave function) and hence the nuclear forces in TDDFT are cast in [1]

$$M_I \frac{\partial^2 R_I}{\partial t^2} = -\int dr \rho(r,t) \nabla_I v_0(r, \mathbf{R}), \tag{4.44}$$

in which

$$\nabla_I v_0(r, \mathbf{R}) = -\nabla_I \sum_I^N \frac{Z_I e^2}{4\pi\epsilon_0 r_{iI}} + \frac{\nabla_I}{n} \sum_{J\neq I}^N \frac{Z_I Z_J e^2}{4\pi\epsilon_0 r_{IJ}}, \tag{4.45}$$

and the other terms vanish as they do not depend on nuclear coordinates.

Briefly, the motions of the nuclei and electronic degrees of freedom are computed "on the fly", where the nuclei are driven by the average field of the electrons whereas the field of the nuclei affects the evolution of the electron density.

[1] which implicitly means that the second term in Equation (4.40) vanishes after applying gradient on the equation

4.5 Born-Oppenheimer molecular dynamics

Born-Oppenheimer MD can be considered to be a simplified variation of Ehrenfest MD, because instead of following non-adiabatically the effective potential energy surface averaged by all states a molecular system in BO MD is subjected to follow a potential energy surface related to a single adiabatic state (typically the electronic ground state). We could derive BO MD by going back to the time-independent wave function formulation in Section 4.1, but it is more convenient to continue from Equation (4.42) that was derived in the previous section:

$$M_I \frac{\partial^2 R_I}{\partial t^2} = -\nabla_I \int d\mathbf{r} \Psi^* H_r \Psi \tag{4.46}$$

Let us expand the electronic wave function in terms of Slater determinants Ψ_i corresponding to different electronic states [32]:

$$\Psi(\mathbf{r}, t; \mathbf{R}) = \sum_{i=0}^{\infty} c_i(t) \Psi_i(\mathbf{r}; \mathbf{R}), \tag{4.47}$$

where a coefficient $c_i(t)$ is the time evolution of the state i occupation ($\sum_{i=0}^{\infty} |c_i(t)|^2 = 1$). When a system is approximated to move only on the ground-state potential energy surface, the total electronic wave function is restricted to the ground state all the time, i.e $c_0(t) = 1$ and the remaining coefficients $c_i(t) = 0$. Consequently, the nuclear forces are simplified to

$$M_I \frac{\partial^2 R_I}{\partial t^2} = -\nabla_I \int d\mathbf{r} \Psi_0^*(\mathbf{r}; \mathbf{R}) H_r(\mathbf{r}; \mathbf{R}) \Psi_0(\mathbf{r}; \mathbf{R}) = -\nabla_I E_0(\mathbf{R}), \tag{4.48}$$

where the term $E_0(\mathbf{R})$ is the ground-state potential energy surface parametrized by the fixed nuclear coordinates.

In brief, (ground-state) BO MD involves solving the stationary electronic structure constrained by the fixed nuclei in every molecular dynamics step, whereas nuclear motions are computed classically from the forces obtained from the negative gradient of the stationary electronic structure energy.

4.6 Car-Parrinello molecular dynamics

Faster and more efficient *ab initio* molecular dynamics methods are more and more in demand as the size of a system of interest grows, yet accuracy cannot be deprecated. Responding to this need, Car and Parrinello [7] came up with a novel molecular dynamics method exploiting density functional theory, where the electronic and ionic degrees of freedom are propagated concurrently. Basically, CP MD can be categorized into the same semi-classical molecular dynamics class as BO MD, but the fundamental difference from BO MD is that the electronic structure re-optimization is avoided in CP MD method. This is possible by introducing the electronic degrees of freedom as fictitious dynamical variables. The equations of motion of two kinds of degrees of freedom can be derived from the Lagrangian:

$$\begin{aligned} L(\psi_i, R_I) =& \frac{1}{2}\sum_i \mu \int \dot{\psi}_i^*(r)\dot{\psi}_i(r)dr + \frac{1}{2}\sum_I M_I|\dot{R}_I|^2 \\ &+ E_{KS}(\psi_i, R_I) + \sum_{ij}\left[\int \psi_i^*(r)\psi_j(r)dr - \delta_{ij}\right]\Lambda_{ji}, \end{aligned} \tag{4.49}$$

where the first term on the r.h.s of Equation (4.49) corresponds to the fictitious electronic kinetic energy functional and μ is a fictitious mass associated with the electronic degrees of freedom. The next term contributes to the ionic kinetic energy, whereas the last term in the same equation with Lagrange multipliers Λ_{ji} ensures orthonormality of the KS orbitals during the dynamics. The resulting equations of motions are:

$$M_I\ddot{R}_I = -\frac{\delta E_{KS}}{\delta R_I} \tag{4.50}$$

$$\mu\ddot{\psi}_i = -H\psi_i(r) + \sum_j \psi_j(r)\Lambda_{ji} \tag{4.51}$$

The electronic equations of motions (Equation (4.51)) is a non-physical device for constructing the electronic structure so that the ionic equations of motions (Equation (4.50)) can be computed in an efficient way.

To summarize this method, in CP MD the burden of the electronic

degrees of freedom re-optimization in molecular dynamics can be avoided by letting the fictitious dynamical variables of electrons propagate in small thickness above the BO potential energy surface of a system. In this sense, an appropriate fictitious mass μ is chosen to ensure the adiabacity of a propagation.

Chapter 5

Results and conclusions

5.1 Resonant Auger electron-photoion coincidence study of the fragmentation dynamics of acrylonitrile molecule (Paper II)

In this study, photofragmentation of gaseous acrylonitrile (C_2H_3-CN) and its deuterated species were studied by means of *ab initio* calculations and PEPICO spectroscopy using synchrotron radiation. Monochromatic synchrotron radiation was used to promote K-shell electrons of nitrogen and carbon from the cyano group (C≡N) to the unoccupied antibonding $\pi^*_{C\equiv N}$ orbital. Photofragmentation of acrylonitrile molecules following selective resonant core excitations was recorded by PEPICO technique. The author adapted *ab initio* calculations to estimate appearance energies of dissociated cationic fragments and to explain geometrical structure rearrangement of acrylonitrile before dissociation. The *ab initio* appearance energies were calculated by subtracting the total energy of the neutral parent compound from the sum of total energies of its isolated fragments. All fragments were supposed to be in the electronic ground state of their respective charge state and, furthermore, in the geometric arrangement corresponding to the lowest-energy isomer.

The above method predicts rather well the appearance thresholds for cations $C_3H_3N^+$ and $C_3H_2N^+$. The molecular geometries for defining the appearance energies are the global minimum geometries which deviate very

little from the geometry structure of the parent molecule. In the case of cation C_3HN^+, the appearance energy provided by the method is underestimated, most probably because the two neutral hydrogens were supposed to depart as H_2 after the ejection of an Auger electron. In addition, the remaining hydrogen in the non-equilibrium singly ionized acrylonitrile was assumed to migrate to the nitrogen end during the dissociation process to attain the global minimum geometry (C_3N-H^+), but this may not take place. The appearance threshold for cation C_3HN^+ would correspond well to the experimental data if geometry of the cation C_3HN^+ is taken to converge to the nearest minima (HC-C-CN^+ or C-CH-CN^+) and the other two hydrogens are assumed to depart as atoms, not as a molecule. In other words, it appears that dissociating fragments frequently do not have enough excess energy to move along their own PESs in order to end up at global minima far from their initial stationary points.

According to the comparison between measurement results of fully deuterated acrylonitrile and non-deuterated acrylonitrile, a mass-to-charge ratio $m/q = 26$ detected in the PEPICO spectroscopy corresponds most likely to cation $C_2H_2^+$ but very rarely to cation CN^+ (assuming that fragmentation dynamics of deuterated species do not differ significantly from the ones of non-deuterated species). Furthermore, mass-to-charge ratios $m/q = 26\,\&\,27$ from experimental results of a singly deuterated acrylonitrile (the central hydrogen is replaced by deuterium) suggest that the hydrogen bonded to the central carbon can be a part of the resulting cation $C_2H_2^+$. Let us assume that theoretical appearance energies combined with experimental ones are suitable for predicting appearance thresholds of fragments with specific geometries (if isomers used for defining the appearance energies are not constrained to be the global minimum isomers). In that case, the equivalent experimental and theoretical appearance energy threshold of deuterated acetylenes (H-C-C-D^+) and normal acetylenes (H-C-C-H^+) dissociated from the singly deuterated acrylonitrile suggests that the precursor molecular cation must undergo geometrical structure rearrangement. More explicitly, an Auger electron leaves the precursor molecular cation in an intermediate state, from which evolution of the electronic structure ne-

cessitates hydrogen migration before molecular dissociation into fragments $HCCH^+$ and HCN takes place. Advanced molecular dynamics calculations may fully verify this speculation, but simple investigations of stationary points already suggest that the dissociation pathways are at least energetically possible. Although the effect of deuteration on the dissociation pathways and dynamics might be underestimated by assuming it to be negligible in the research paper, the energy barriers in the modelled dissocation pathways resulting in fragments $HCCH^+$ and HCN from the non-deuterated and singly deuterated non-equilibrium parent cations should not differ significantly.

In conclusion, appearance energy estimation based on the aforementioned total energy subtraction of the parent molecule and its fragment provides values in good agreement with the experimental data. The method would give values corresponding to the thresholds in CIY spectra more accurately if *ab initio* appearance energy definition were based on the total energies of local minimum geometries close to the initial geometries. In hindsight, other than global minimum isomers should have been taken into account in computing appearance energy, which could better explain the maxima related to different cationic fragments plotted in CIYs in the article.

5.2 Fragmentation patterns of core ionized uracil, 5-bromouracil and thymine (Paper I & III)

Photofragmentation of core ionized biomolecules: uracil, 5-bromouracil and thymine, has been studied by applying PEPIPICO spectroscopy with synchrotron radiation in these papers. *Ab initio* calculations were adapted to investigate correlation between intensities of observed dissociated cationic fragments and their theoretical appearance energies. The appearance energies were estimated by subtracting the total energies of fragments from a parent neutral molecule as was done in Paper II .

The PIPICO patterns of thymine correspond to fewer fragmentation channels than the ones of uracil, which obviously implicates some correla-

tion between the intensities of the PIPICO patterns and the theoretical appearance energies of the cationic fragments derived from the corresponding PIPICO patterns in the case of thymine but not of uracil. An added complexity is that a single detected channel defined by mass-to-charge ratios of ions can correspond to multiple fragment combinations in both molecules, which confuses the meaning of the appearance energy. In any case, the bad overall correlation suggests that the decay rates into the major fragmentation channels are not governed by the fragment products in their optimal geometries but rather by complex electronic transitions leading to the final electronic states and the associated molecular dynamics.

In summary, possible correlation between observed dissociated cationic fragments and appearance energy values should be investigated only in the cases of a small system with simple fragmentation mechanisms, and even then the investigation strategy itself gives an indirect correlation information between dissociation pathways and appearance energies. That is to say, after ejection of Auger electrons, molecular fragmentation is likely to be dictated by a large amount of doubly charged final states and their associated molecular dynamics of a complex system. Thus, neglecting the role of intermediate molecular states cannot give a very accurate picture of fragmentation processes.

5.3 Experimental and *ab initio* study of the photofragmentation of DNA and RNA sugars (Paper IV)

This research paper comprises photodissociation study on core ionized D-ribose ($C_5H_{10}O_5$, the RNA sugar) and 2-deoxy-D-ribose ($C_5H_{10}O_4$, the DNA sugar) molecules and the isotopically labelled samples (see Figure 5.1) by means of PEPICO spectroscopy and synchrotron radiation. Binding energies of C 1s in different chemical environments of the molecules recorded in photoelectron spectra were resolved in theoretical modelling by adapting Koopman's theorem [21]. In this study we have discovered that irradiating DNA/RNA sugars with soft X-rays (here 330 eV and 578 eV) will cause

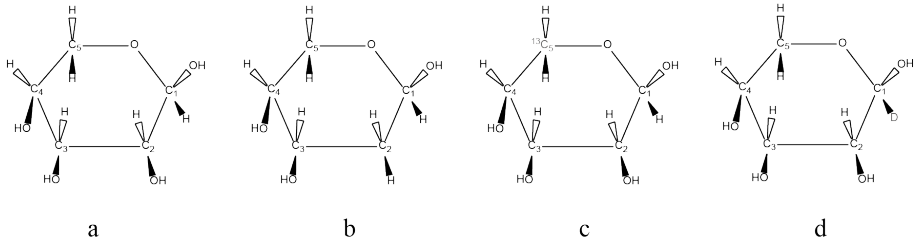

Figure 5.1: D-ribose (a), 2-deoxy-D-ribose (b), D-ribose with C(5) is isotopically labelled c) and deuterated D-ribose (d).

them to essentially explode into small fragments where the heaviest cationic fragment is 43 amu ($C_2H_3O^+$). The fragmentation mechanism induced by the core C 1s and O 1s level ionization of DNA sugar does not differ much from the one of RNA sugar. DNA sugar, with an additional HCH group compared to RNA sugar, enables the production of the (CH_3^+ (15), $C_2H_3^+$ (27)) and (CHO^+ (29), $C_3H_3^+$ (39)) ion pairs, which is not possible with RNA sugar. Otherwise, the characteristic dissociation channels of both sugars involve either a loss of a hydroxyl (-OH) group and/or a capture or a loss of a hydrogen atom. In addition, bond cleavages in the dissociation processes involve any ring location in the pyranoses. In practice, this violent molecular explosion tends to strip the ring bonds of a molecule down to its fundamental building blocks, i.e. the HCH and HCOH groups. However, as cation the $HCOH^+$ radical/group is prone to eject a hydrogen atom in order to gain a more stable cationic form, HCO^+. Heavier cationic fragments, such as $C_2H_2O^+$ (42) and $C_2H_3O^+$ (43), formed by different combinations of the basic building blocks are also rather common dissociation products.

According to the *ab initio* calculations performed, the O-H bond has a higher tendency to eject a hydrogen than the C-H bond in $CH_2O^+ \rightarrow CHO^+$ & H, which suggests that the O-H bond would break more easily than the C-H bond in the fragmentation processes of the doubly charged sugar molecules. This could be verified by studying suitably deuterated samples.

In general, the fragmentation patterns of D-ribose and 2-deoxy-D-ribose

can be summarized to involve the following general steps (see Figure 5.2):

- The HCOH group (see Figure 5.2a) serves as a precursor moiety creating aldehyde cations by dissipating a hydrogen from the hydroxyl group, or capturing a hydrogen atom from a neighbouring group during the fragmentation process to yield CH_3O^+.
- The HCH (14) moiety (see Figure 5.2b) has a tendency to separate intact and it can also capture a hydrogen from a neighbouring HCOH moiety resulting in CH_3^+ (15).
- The moiety shown in Figure 5.2c can produce $C_2H_3O^+$ (43) by losing a hydrogen from the hydroxyl group, and $C_2H_2O^+$ (42) by ejecting an additional hydrogen from the HCH group. Furthermore, the same moiety can produce $C_2H_3^+$(27) by ejecting a whole hydroxyl group, and $C_2H_4^+$(28) by recapturing the hydrogen atom from the eliminated hydroxyl group.
- The moieties shown in Figure 5.2d are capable of producing $C_2H_3O^+$ (43) by ejecting a hydroxyl radical and $C_2H_2O^+$ (42) by losing a hydroxyl group and a hydrogen atom from another hydroxyl group, possibly in the form of H_2O (commonly known as water elimination).

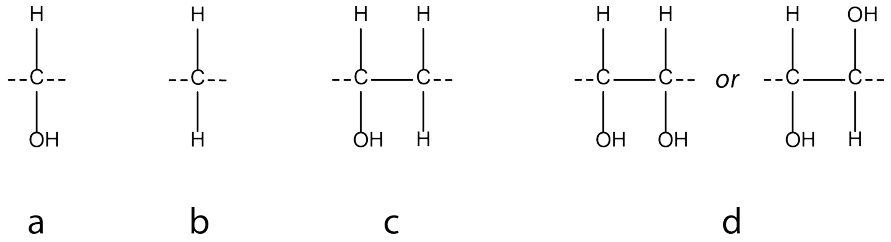

Figure 5.2: Different moieties (as cation fragments) of the parent molecular ions involved in the different fragmentation pathways (see text).

In conclusion, with the dissociation mechanisms described above, one can expect the consequences of soft X-ray irradiation to be lethal to DNA

/RNA helix, especially considering the fragments departing from the carbon C(3) and C(5) sites which are connected to the phosphate backbone in DNA/RNA chain. It is possible that the cations of the dissociated sugar stay bonded with adjacent phosphates and, therefore, due to their non-thermal kinetic energy, attempt to pull the phosphates or parts of the phosphates out of their locations causing additional damage to the helix. More likely, however, the cationic fragments thrust out from their location tearing also the bonds of the adjacent phosphates, and may collide with other adjacent parts of the DNA/RNA helix, creating damage clusters. Either way, soft X-ray damage is likely to lead to multiple and clustered strand breaks in the DNA/RNA helix. This might be valid for DNA/RNA helices clustered in a small area (thus minimizing the space between parts of the helices). However, moieties in DNA/RNA helices far from the Coulomb explosion points are well protected (by water molecules filling the space in biological environments) from the cationic fragments according to Liu et al. [28].

5.4 Size selective spectroscopy of Se microclusters (Paper V)

This research paper reports the electronic structure and photofragmentation study of Se_n microclusters ($n \leqslant 8$) by means of *ab initio* methods and size-selective PEPICO technique with VUV synchrotron radiation. The clusters were produced by direct vacuum evaporation, therefore the exact sizes and conformations of the produced clusters could not be controlled. The recorded data was presented in forms of a PEPICO map, PIY and coincident ion yield (CIY) for interpretation. The author applied *ab initio* calculations to bring additional aspects into the study.

Based on the TOF and PIY spectrum of selenium clusters (Se_{2-8}) obtained at the photon energy of 10 eV, signals of Se_3^+ and Se_4^+ cations are weak and their experimental appearance energy thresholds are rather high compared to selenium cluster ions of other sizes. In addition, the CIY spectra recorded at the photon energy of 22 eV suggests that the Se_3 and

Se_4 clusters are hardly formed at all under the direct evaporation circumstances and that the Se_3^+ and Se_4^+ cations detected are instead of cationic fragments dissociated from bigger microclusters. Inspection of the CIY spectra of Se_6^+ and Se_7^+ also suggests that removal of electrons from molecular orbitals below certain energy levels (typically $E \leqslant -10$ eV) results in fragmentation into smaller clusters, such as the aforementioned Se_3^+ and Se_4^+ cationic fragments.

In the *ab initio* contribution, we modelled microclusters for different molecular geometries of the cluster sizes detected in the measurements. The *ab initio* binding energies of the modelled clusters determined by adopting Koopmans' theorem were contrasted with the experimental binding energies via the CIY spectra. As Se_2 has only one equilibrium molecular geometry, the CIY spectrum of Se_2^+ can be used as reference for verifying the theoretically defined binding energies, and indeed the theoretical values match well with the peaks in the CIY spectrum of Se_2^+. Further comparison between the theoretical and experimental binding energy values of bigger clusters implicitly supports the idea that the Se_6 and Se_7 clusters produced in the measurements are prone to dissociate into smaller fragments after removal of an inner valence electron and that the Se_3^+ and Se_4^+ cations detected are mainly cationic fragments dissociated from bigger clusters.

To sum up, although Koopmans' theorem suffers from the frozen orbital approximation, the predicted binding energy values agree qualitatively well with the experimental data expressed in the CIY spectrum of at least Se_2^+ cations. Given that the theorem also holds for clusters a few atoms larger, Koopmans' theorem provides a simple and interesting way to extract useful information from the *ab initio* results in order to support the experimental data interpretation.

5.5 Fragmentation Dynamics of Doubly Charged Methionine in the Gas Phase (Paper VI)

In the research, photofragmentation of gaseous methionine (see Figure 5.3) was studied by means of Auger electron photo-ion photo-ion coincidence

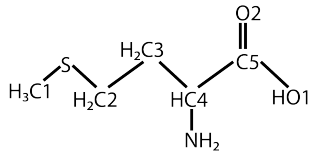

Figure 5.3: Simplified molecular geometry of methionine with carbon and oxygen atoms enumerated.

(AEPIPICO) spectroscopy and *ab initio* calculations. Experimentally, two photo-ions were measured concurrently with S LMM Auger electrons after irradiating methionine by using monochromated synchrotron radiation. *Ab initio* methods were adopted to simulate a S LMM Auger spectrum (see Figure 5.4) in order to link experimental fragmentation data and theoretical results. In addition, nuclear motions of non-equilibrium doubly charged methionine were studied by adapting *ab initio* molecular dynamics (MD) methods. The Ehrenfest MD (EMD) associated with the time-dependent density functional theory (TDDFT) [44] suits perfectly this research objective, because the method enables propagating electronic structure and nuclear motions of doubly charged molecules starting from the Auger final states. However, since the TDDFT EMD method requires excessive computational resources, it is advisable to continue the TDDFT EMD trajectories by using Born-Oppenheimer MD method when the dynamics of both methods are essentially adiabatic. Lastly, the fast but accurate Car-Parrinello (CP) MD method was also used to perform a 5 ps equilibration process and to model fragmentation channels of doubly charged methionine in the ground state with various initial temperatures. The purpose of adding initial temperatures is to attempt to compensate the relaxation energies of doubly charged methionine from the Auger final states to the ground state. The procedure is by no means a substitute for the role of the TDDFT EMD calculations, since it is not possible to propagate the electronic structure of doubly charged methionine from the Auger final states by using the CP MD method. Nevertheless, the procedure gives an idea of different dissociation channels of doubly charged methionine molecules, which renders another

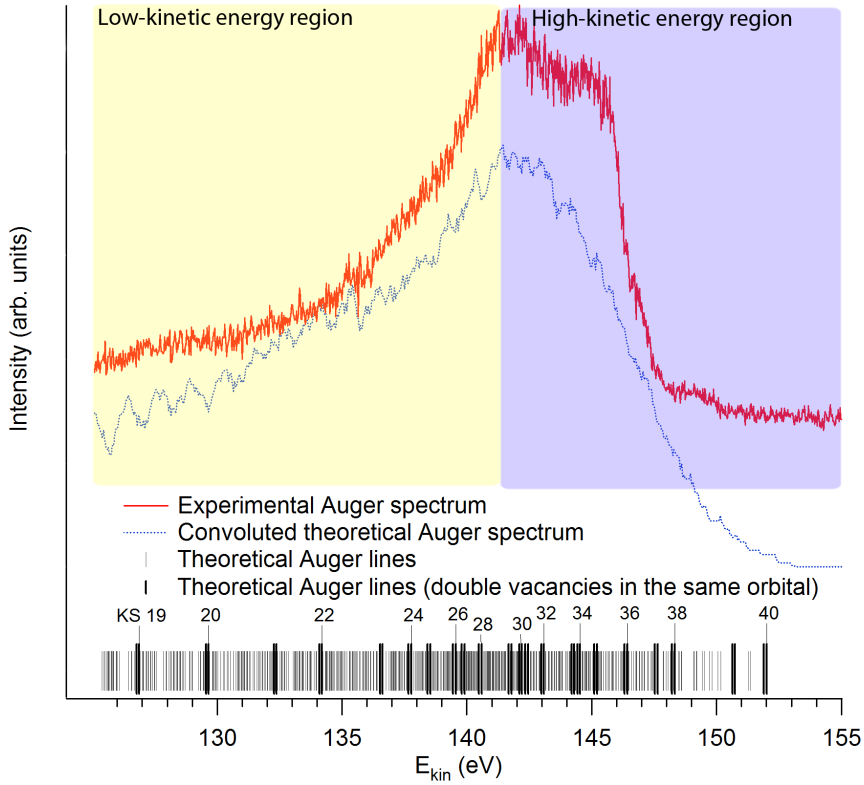

Figure 5.4: The measured S LMM Auger electron spectrum of methionine (red curve). Grey vertical short bars represent kinetic energies of emitted Auger electrons leaving behind all possible combinations of vacancy orbitals forming different non-equilibrium M^{2+} molecules after S $2p$ ionizations, whereas long vertical black bars correspond to kinetic energies of emitted Auger electrons corresponding to two holes in the same orbital. The convoluted theoretical Auger spectrum (blue dashed curve) is a smoothed histogram of the theoretical Auger lines and has been shifted by -15 eV.

aspect on the current research in addition to the experimental method.

TDDFT EMD results

The TDDFT EMD, in principle, offers a powerful means to model molecular dynamics of the system of interest, but the method requires high computational resources and is very time consuming. Therefore, any strategy

relieving the computational burden is desirable, one of which is an attempt to bring the computation to a manageable level that still retains the qualitative information of the dynamics, e.g. by choosing the optimal time step for the simulations. With this in mind, two simulations with two different time steps, ts = 0.24 as and ts = 0.60 as, were executed in order to find the optimal time step. The TDDFT EMD simulations begin from a non-equilibrium doubly charged methionine where two electrons are removed from the Kohn-Sham (KS) orbital 36 (HOMO-4) (Figure 5.5), which belongs to high-kinetic energy region in the Auger spectra (Figure 5.4).

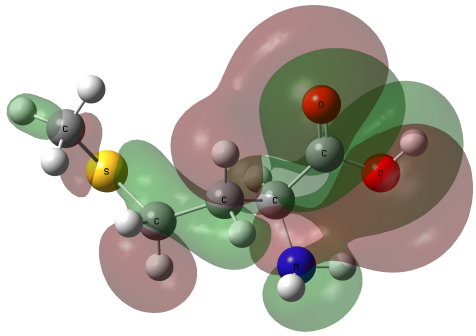

Figure 5.5: KS orbital 36 of methionine.

The comparison results are shown in Figures 5.6(a), 5.6(b), 5.7 and 5.8. The curves in Figure 5.6(a) plot Kohn-Sham energies of the doubly charged methionine as function of time, whereas the ones in Figure 5.6(b) plot the temperatures (average kinetic energies of nuclear degrees of freedom) as function of time. The curves in Figure 5.7 draw the sums of the previous two physical quantities, i.e. the total energies of the dynamical systems, which can be used as qualitative judgement of a TDDFT EMD simulation for a given time step by monitoring the total energy conservation of the system.

Although total energy of the system varies as much as 2.288 eV at 58 fs in the bigger time steps, trajectories (see Figure 5.8) simulated with the

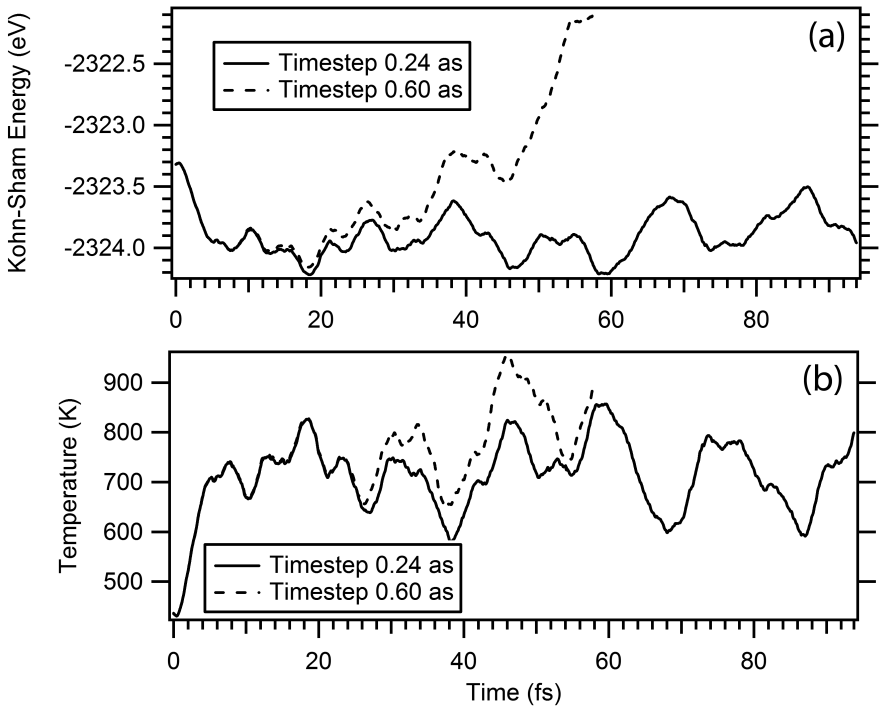

Figure 5.6: Time step comparison for (a) Kohn-Sham energies (b) temperatures in the TDDFT EMD simulations of a non-equilibrium doubly charged methionine with an empty KS orbital 36.

bigger time step deviate slightly from the ones with small time step. In this sense, systems dissociating at that time scale may be simulated with the bigger time step to obtain qualitative results with caution. In slower fragmentation cases, simulations should be run with the smaller time step in order to retrieve accurate results.

In addition to propagating the electronic structure of the non-equilibrium doubly charged methionine with the empty KS orbital 36, the case of an empty KS orbital 19 (Figure 5.9) has been inspected. The orbital was chosen for its partial overlapping with a S $2p$ orbital and its matching of the low-kinetic energy range in the Auger spectra (Figure 5.4). The trajec-

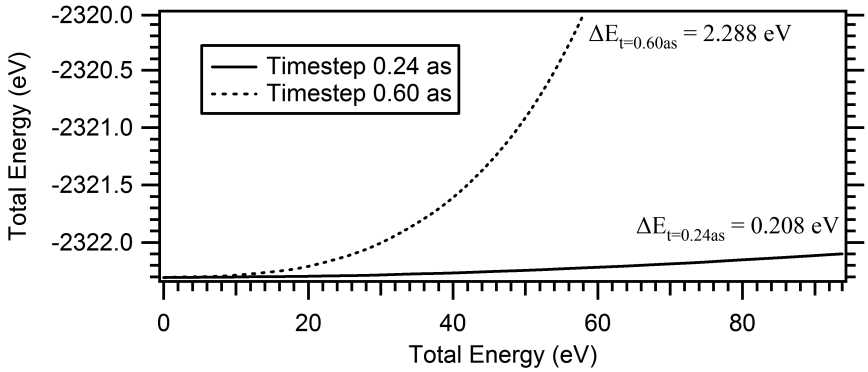

Figure 5.7: Time step comparison for total energies in the TDDFT EMD simulations of a non-equilibrium doubly charged methionine with an empty KS orbital 36. Total energy change in the simulation of the time step ts = 0.60 as is 2.288 eV at 58 fs and 0.208 eV in the one of the smaller time step at 93 fs.

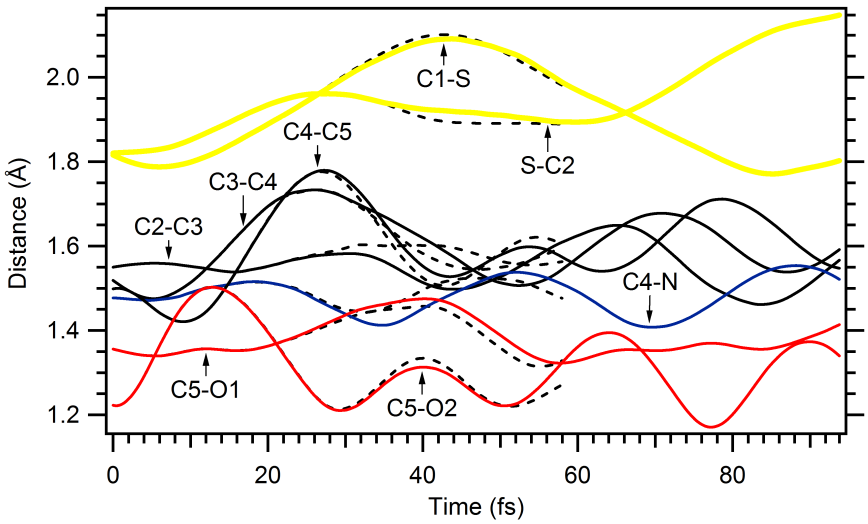

Figure 5.8: Bond lengths in the TDDFT EMD simulations of a non-equilibrium doubly charged methionine with an empty KS orbital 36. Dashed lines denote bond lengths in the TDDFT EMD simulation with the time step ts = 0.60 as, and continuous lines represent the ones in the TDDFT EMD simulation with the time step ts = 0.24 as.

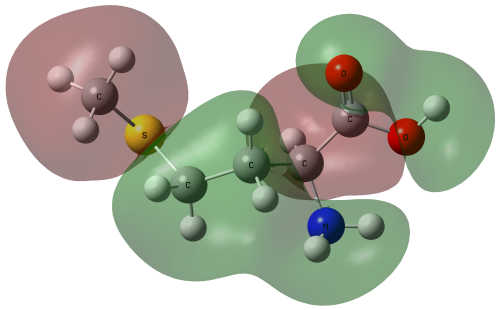

Figure 5.9: KS orbital 19 of methionine.

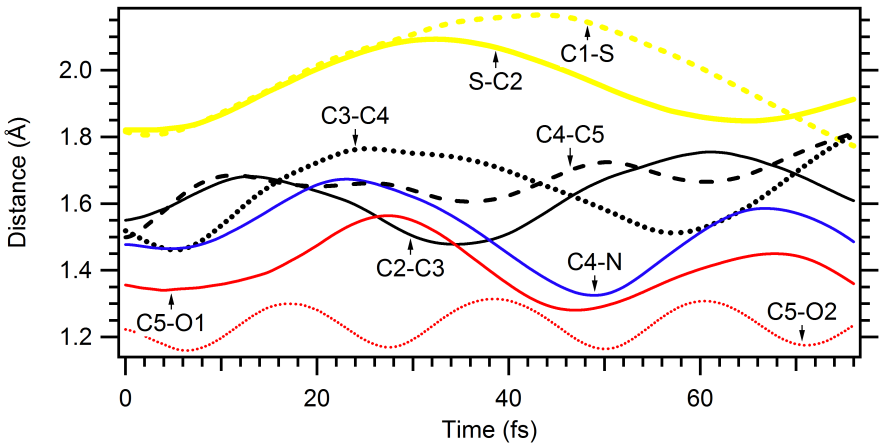

Figure 5.10: Bond lengths of a non-equilibrium doubly charged methionine with an empty KS orbital 19, propagated with the time step ts = 0.24 as.

tories in Figure 5.10 imply that methionine in this case does not seem to dissociate at around 70 fs, hence the simulation has to be extended.

KS orbital 14 (Figure 5.11) is low in energy and particularly tightly localized at the COOH moiety. The KS orbital 14 does not overlap with the S $2p$ orbitals, and therefore a non-equilibrium doubly charged state with an empty KS orbital 14 may not be a consequence of S $2p$ photo-

ionization. Nevertheless, considering the molecular dynamics of methionine from a general aspect, molecular fragmentation of a non-equilibrium doubly charged methionine, where two electrons are removed from a low energy and tightly localized orbital, may behave in a radical way in comparison with the cases of KS orbital 19 or 36. For this purpose, we also performed TDDFT EMD calculations on the case of doubly vacant KS orbital 14.

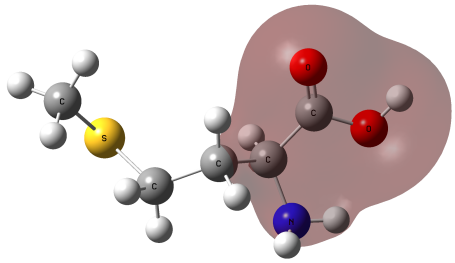

Figure 5.11: KS orbital 14 of methionine.

Results of the TDDFT EMD simulation (using the time step ts = 0.60 as) in the case of an empty KS orbital 14 are presented in Figures 5.12 and 5.13. The temperature curve in Figure 5.12 shows ultra-fast heat increase over 2500 K already at 5 fs and the trajectories in Figure 5.13 suggest that molecular dissociation also occurs very early. The two "M" shapes in the temperature curve at 31 fs and 45 fs correspond to strong attractive and repulsive interactions of hydrogen in the vicinity of oxygen O1. Figure 5.14 illustrates the dissociation at 51.7 fs. In reality, the rapid fragmentation would correspond to the case in which doubly charged methionine (after Auger electron emission) relaxes directly to a dissociation state. The case is appealing and studying it should not consume computational resources tremendously, hence the related TDDFT EMD calculations ought to be performed with the smaller time step in order to attain more accurate results.

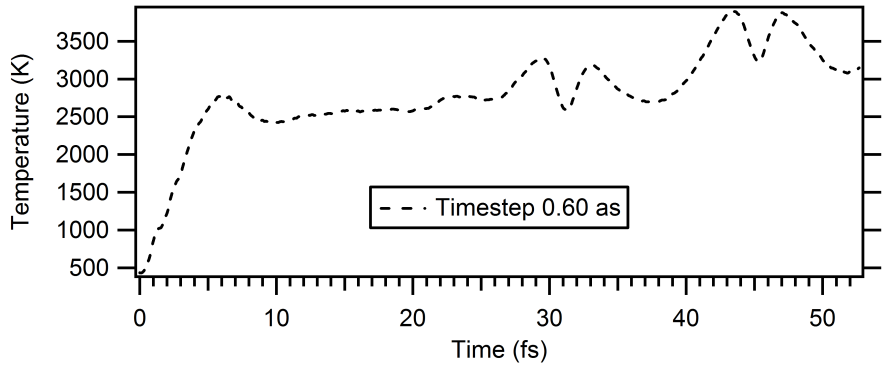

Figure 5.12: The temperature curve in the TDDFT EMD simulation of a non-equilibrium doubly charged methionine with an empty KS orbital 14.

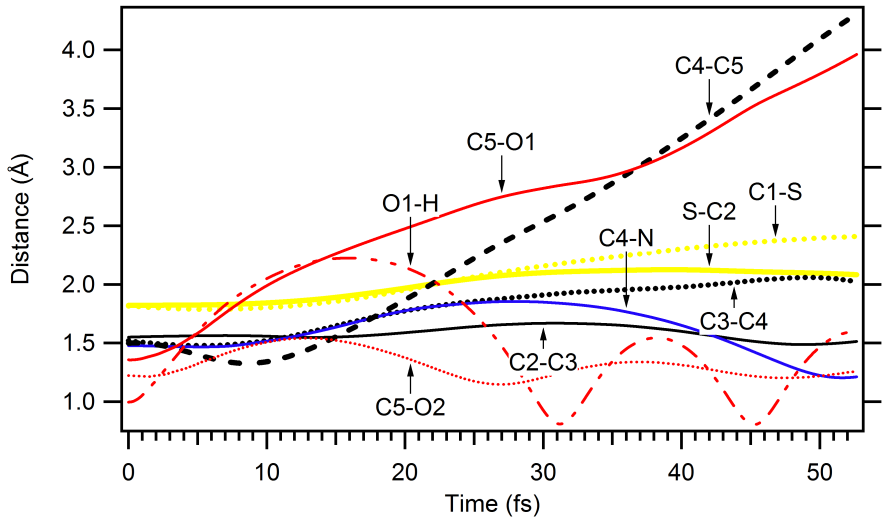

Figure 5.13: Bond lengths of a non-equilibrium doubly charged methionine with an empty KS orbital 14, propagated with the time step ts = 0.60 as.

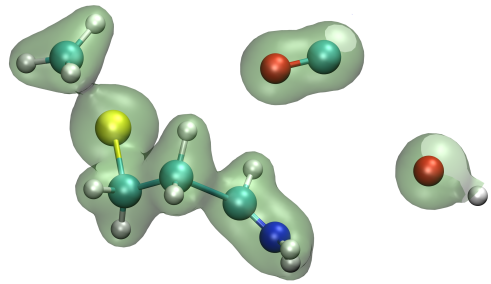

Figure 5.14: Fragmentation of doubly charged methionine (with the empty KS orbital 14) at t = 51.7 fs in the TDDFT EMD simulation. Bader [43] charge analysis shows that the charge of the departing methyl radical is roughly 0.5 and the fragments CO and OH are practically neutral.

In summary, the TDDFT EMD time step comparison in this work suggests that simulations of doubly charged methionine with an empty KS orbital of a high energy level should be executed with the time step ts = 0.24 as or with a smaller one in order to obtain reliable results. According to the TDDFT EMD calculations, the electronic structure of non-equilibrium doubly charged methionine molecules with either empty KS orbital 19 or KS orbital 36 does not relax directly to a dissociation state, but the evolution of the electronic structure necessitates the associated molecular system to vibrate intensively in the first 50 fs or so. The simulations must be extended for a longer period time in order to gain a good picture of the molecular dynamics of doubly charged methionine. As the research based on the TDDFT EMD method alone is an extensive study, it will be published separately. Hence, Paper VI includes the other *ab initio* calculations and experimental results.

Experimental and Car-Parrinello MD results

Based on the experimental results, the photofragmentation of methionine can be explained consistently by one general scenario of nuclear dynamics:

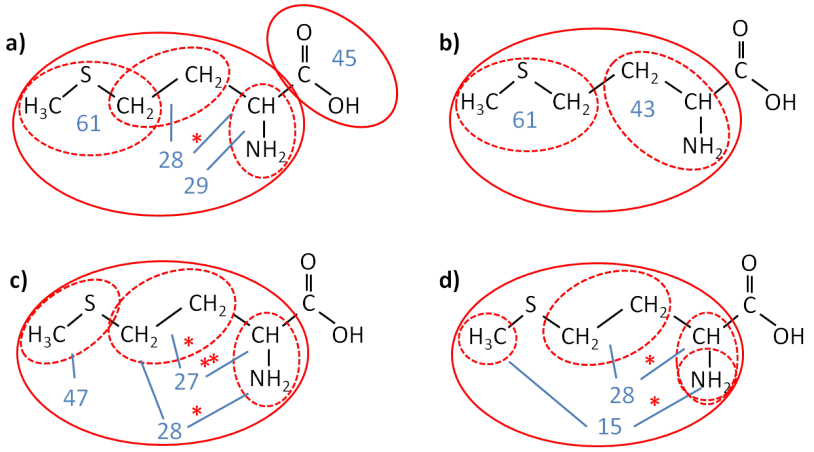

Figure 5.15: Dissociation channels for methionine. Solid red circles: charged fragments after primary stage. Dashed red circles: secondary dissociation charged fragments. Stars mark hydrogen loss and numbers fragment masses.

a) Carboxyl radical separates either carrying charge (Figure 5.15a) or being neutral (Figure 5.15b, 5.15c and 5.15d). None of the observed patterns indicate secondary dissociation of the cationic carboxyl radical.

b) The remaining part of the molecule always dissociates further into fragments ranging in size from mass 61 to 15.

c) There is the possibility of hydrogen loss or transfer accompanying these processes.

The intensity of various fragmentation channels depends on the electronic states of the parent dication in two very distinctly different ways: In the first case the heaviest fragment pairs (CH_2-CH-NH_2^+, CH_3-S-CH_2^+) and

($COOH^+$, CH_3-S-CH_2^+) are correlated only with the Auger electrons of high kinetic energy. These channels are thus open only for the electronic states with vacancies in weakly bound MOs. As they require the least amount of broken bonds, these channels are also least energy-consuming. However, no fragmentation channel with minimal damage (two-body process) was observed. In the second case, the lighter cation pairs are observed in coincidence with Auger electrons with the kinetic energy across the entire spectrum (127 - 151 eV), although the yields are stronger for higher-lying electronic states.

In the *ab initio* part, CP MD method was applied to performing nuclear motions of doubly charged methionine in the ground state with various initial temperatures ranging from 3630 K to 19896 K. The C4-C5 bond breakage is observed in all cases. In the lowest temperatures the C4-C5 bond breakage results in either a charged or a neutral carboxyl radical. In these cases, further dissociation was not observed during the 300 fs time propagation. However, it cannot be excluded that this process might occur after a long time (from a few hundred femtoseconds to picoseconds after the C4-C5 bond scissoring). In intermediate temperatures, singly charged carboxyl detachment is followed by C2-C3 bond cleavage resulting in fragments COOH (m = 45), CH_2-CH-NH_2^+ (m = 43) and CH_3-S-CH_2^+ (m = 61). At the highest temperatures, fragmentation begins in less than 20 fs. The dissociation involves some isomerisation, hydrogen capture and loss.

It is notable that the sequence of fragmentation dynamics that emerged from the experiment is supported by the CP MD simulations – in both theory and experiment the separation of the carboxyl group always occurs, the cationic fragment CO^+ is not observed. Also, the dissociation channel producing the fragments COOH (m = 45), CH_2-CH-NH_2^+ (m = 43) and CH_3-S-CH_2^+ (m = 61) in the CP MD simulations is consistent with the experimental result concerning the ion pair (43,61). In order to get a much deeper understanding of the fragmentation pathways starting from the deeper Auger final states, it would be desirable to extend the present theoretical framework to TDDFT EMD calculations.

5.6 Final words

The issue of molecular fragmentation induced by synchrotron radiation can be successfully studied by the PEPICO technique and *ab initio* methods. The PEPICO technique provides crucial data on changes in the electronic structure and final ionic chemical compositions of a system, although it does not give a complete picture comprising all phases starting from the first moment of the photon-matter interaction and ending in possible molecular fragmentation. To this end, *ab initio* calculations complement the experiments by bringing information on the evolution of the electronic structure of a system subjected to irradiation. Furthermore, computational quantum chemistry provides independent methods to study electronic structure and molecular dynamics of a system. The *ab initio* results of this work can be improved by more thorough calculations which require many detailed calculation steps. The advanced calculations would include *i.a.* computing electronic state transitions, and a computing strategy which does not average potential energy surfaces (in TDDFT-EMD) but allows the system to jump from a single adiabatic surface to another according to the dictating states at a certain point on the corresponding PESs such as in *Tully surface hopping* method [39]. All in all, combining the experimental technique and the *ab initio* methods creates a powerful tool for understanding molecular fragmentation induced by synchrotron radiation.

Interaction of a molecular system with VUV or soft X-ray light changes the electronic structure of the system and is capable of causing chemical bond breakage if the evolution of the electronic structures necessitates that. Bond breakage sites are not always trivial, since the relaxation of an electronic structure interacted with light can end up to various states dictating the associated molecular dynamics. Moreover, fragmentation processes do not necessarily follow the energetically most favourable pathways resulting in fragments with globally optimized geometries, but the dissociation pathways seem to be mainly characterized by the final state of the parent molecule and perhaps state populations determining the dominating potential energy surfaces.

References

[1] José L. Alonso, Alberto Castro, Pablo Echenique, and Angel Rubio. On the combination of tddft with molecular dynamics: New developments. In Miguel A.L. Marques, Neepa T. Maitra, Fernando M.S. Nogueira, E.K.U. Gross, and Angel Rubio, editors, *Fundamentals of Time-Dependent Density Functional Theory*, volume 837 of *Lecture Notes in Physics*, pages 301–315. Springer Berlin Heidelberg, 2012. ISBN 978-3-642-23517-7. doi: 10.1007/978-3-642-23518-4_15. URL http://dx.doi.org/10.1007/978-3-642-23518-4_15. 53

[2] D. Attwood. *Soft X-rays and extreme ultraviolet radiation: principles and applications*. Cambridge University Press, 1999. 25, 28

[3] P. Auger. Sur les rayons secondaires produits dans un gaz par des rayons x. *C.R.A.S.*, 177:169–171, 1923. 19

[4] R. Baragiola. *Electronic Properties - Lecture Notes*. University of Virginia, USA, 2002. URL http://http://www.virginia.edu/ep/SurfaceScience/electron.html. 19, 21

[5] M. Bässler, A. Ausmees, M. Jurvansuu, R. Feifel, J.-O. Forsell, P. de Tarso Fonseca, A. Kivimäki, S. Sundin, S.L. Sorensen, R. Nyholm, O. Bjrneholm, S. Aksela, and S. Svensson. Beam line i411 at max ii performance and first results. *Nuclear Instruments and Methods in Physics Research Section A: Accelerators, Spectrometers, Detectors and Associated Equipment*, 469(3):382 – 393, 2001. ISSN 0168-9002. doi: 10.1016/S0168-9002(01)00786-0. URL http://www.sciencedirect.com/science/article/pii/S0168900201007860. 29

[6] M. Born and R. Oppenheimer. Zur quantentheorie der molekeln. *Annalen der Physik*, 389(20):457–484, 1927. ISSN 1521-3889. doi: 10.1002/andp.19273892002. URL http://dx.doi.org/10.1002/andp.19273892002. 38

[7] R. Car and M. Parrinello. Unified approach for molecular dynamics and density-functional theory. *Phys. Rev. Lett.*, 55:2471–2474, Nov 1985. doi: 10.1103/PhysRevLett.55.2471. URL http://link.aps.org/doi/10.1103/PhysRevLett.55.2471. 55

[8] C. J. Cramer. *Essentials of Computational Chemistry: Theories and Models*. John Wiley & Sons, England, 2004. 38, 41, 42, 44, 46

[9] A. Einstein. ber einen die erzeugung und verwandlung des lichtes betreffenden heuristischen gesichtspunkt. *Annalen der Physik*, 322(6): 132–148, 1905. ISSN 1521-3889. doi: 10.1002/andp.19053220607. URL http://dx.doi.org/10.1002/andp.19053220607. 14

[10] F. R. Elder, A. M. Gurewitsch, R. V. Langmuir, and H. C. Pollock. Radiation from electrons in a synchrotron. *Phys. Rev.*, 71:829–830, Jun 1947. doi: 10.1103/PhysRev.71.829.5. URL http://link.aps.org/doi/10.1103/PhysRev.71.829.5. 28

[11] M. J. Frisch, G. W. Trucks, H. B. Schlegel, ..., and J. A. Pople. Gaussian 03, Revision C.02. Gaussian, Inc., Wallingford, CT, 2004. 13

[12] D. T. Ha, M. A. Huels, M. Huttula, S. Urpelainen, and E. kukk. Experimental and *ab initio* study of the photofragmentation of dna and rna sugars. *Phys. Rev. A*, 84:033419, Sep 2011. doi: 10.1103/PhysRevA.84.033419. URL http://link.aps.org/doi/10.1103/PhysRevA.84.033419. 10

[13] G. G. Hall. The molecular orbital theory of chemical valency. viii. a method of calculating ionization potentials. *Proceedings of the Royal Society of London. Series A. Mathematical and Physical Sciences*, 205(1083):541–552, 1951. doi: 10.1098/rspa.1951.

0048. URL http://rspa.royalsocietypublishing.org/content/205/1083/541.abstract. 41

[14] H. Hertz. Ueber einen einfluss des ultravioletten lichtes auf die electrische entladung. *Annalen der Physik*, 267(8):983–1000, 1887. ISSN 1521-3889. doi: 10.1002/andp.18872670827. URL http://dx.doi.org/10.1002/andp.18872670827. 14

[15] P. Hohenberg and W. Kohn. Inhomogeneous electron gas. *Phys. Rev.*, 136:B864–B871, Nov 1964. doi: 10.1103/PhysRev.136.B864. URL http://link.aps.org/doi/10.1103/PhysRev.136.B864. 44

[16] M. Huttula, S. Heinäsmäki, H. Aksela, E. Kukk, and S. Aksela. Multielectron effects in 4p photoionization of atomic cs. *Journal of Electron Spectroscopy and Related Phenomena*, 156-158(0):270 – 273, 2007. ISSN 0368-2048. doi: 10.1016/j.elspec.2006.11.018. URL http://www.sciencedirect.com/science/article/pii/S0368204806001691. 26

[17] E. Itälä, D. T. Ha, K. Kooser, E. Rachlew, M. A. Huels, and E. Kukk. Fragmentation patterns of core-ionized thymine and 5-bromouracil. *The Journal of Chemical Physics*, 133(15):154316, 2010. doi: 10.1063/1.3505140. URL http://link.aip.org/link/?JCP/133/154316/1. 10

[18] E. Itälä, D.T. Ha, K. Kooser, E. N ommiste, U. Joost, and E. Kukk. Fragmentation patterns of core ionized uracil. *International Journal of Mass Spectrometry*, 306(1):82 – 90, 2011. ISSN 1387-3806. doi: 10.1016/j.ijms.2011.07.006. URL http://www.sciencedirect.com/science/article/pii/S1387380611002600. 10

[19] George B. Kaufman. Inorganic chemistry: principles of structure and reactivity, 4th ed. (huheey, james e.; keiter, ellen a.; keiter, richard l.). *Journal of Chemical Education*, 70(10):A279, 1993. doi: 10.1021/ed070pA279.1. URL http://pubs.acs.org/doi/abs/10.1021/ed070pA279.1. 15

[20] W. Kohn and L. J. Sham. Self-consistent equations including exchange and correlation effects. *Phys. Rev.*, 140:A1133–A1138, Nov 1965. doi: 10.1103/PhysRev.140.A1133. URL http://link.aps.org/doi/10.1103/PhysRev.140.A1133. 44

[21] T. Koopmans. über die zuordnung von wellenfunktionen und eigenwerten zu den einzelnen elektronen eines atoms. *Physica*, 1(1-6): 104 – 113, 1934. ISSN 0031-8914. doi: 10.1016/S0031-8914(34)90011-2. URL http://www.sciencedirect.com/science/article/pii/S0031891434900112. 60

[22] K. Kooser, D. T. Ha, S. Granroth, E. Itälä, L. Partanen, E. N ommiste, H. Aksela, and E. Kukk. Resonant auger electron photoion coincidence study of the fragmentation dynamics of an acrylonitrile molecule. *Journal of Physics B: Atomic, Molecular and Optical Physics*, 43(23): 235103, 2010. URL http://stacks.iop.org/0953-4075/43/i=23/a=235103. 10

[23] K. Kooser, D. T. Ha, E. Itälä, J. Laksman, S. Urpelainen, and E. Kukk. Size selective spectroscopy of se microclusters. *The Journal of Chemical Physics*, 137(4):044304, 2012. doi: 10.1063/1.4737633. URL http://link.aip.org/link/?JCP/137/044304/1. 10

[24] E. Kukk. *PEPICO data analysis - Software for Igor Pro - User's manual*. University of Turku, Finland, 2007. 29, 31

[25] E. Kukk. *Electron and ion spectroscopy - Lecture Notes*. University of Turku, Finland, 2008. 26, 27, 28

[26] Werner Kutzelnigg. Friedrich hund and chemistry. *Angewandte Chemie International Edition in English*, 35(6):572–586, 1996. ISSN 1521-3773. doi: 10.1002/anie.199605721. URL http://dx.doi.org/10.1002/anie.199605721. 15

[27] A. R. Leach. *Molecular Modelling: Principles and Applications, second edition*. Pearson Education EMA, 2001. 40, 41

[28] B. Liu, S. Brøndsted Nielsen, P. Hvelplund, H. Zettergren, H. Cederquist, B. Manil, and B. A. Huber. Collision-induced dissociation of hydrated adenosine monophosphate nucleotide ions: Protection of the ion in water nanoclusters. *Phys. Rev. Lett.*, 97:133401, Sep 2006. doi: 10.1103/PhysRevLett.97.133401. URL http://link.aps.org/doi/10.1103/PhysRevLett.97.133401. 63

[29] P. López-Tarifa. *Ph.D. Thesis: Fragmentation dynamics of biomolecules in gas phase and water environment.* Universidad Autónoma de Madrid, Madrid, 2011. 50

[30] G. Margaritondo. *Introduction to synchrotron radiation.* Oxford University Press, New York, 1988. 25, 28

[31] M. A. L. Marques and E. K. U. Gross. A primer in density-functional theory. 620, 2003. 48, 49

[32] Dominik Marx and Jrg Hutter. Ab initio molecular dynamics: Theory and implementation. In *MODERN METHODS AND ALGORITHMS OF QUANTUM CHEMISTRY, JOHN VON NEUMANN INSTITUTE FOR COMPUTING, FORSCHUNGSZENTRUM JULICH, 2000*, pages 329–477, 2000. 50, 54

[33] R. S. Friedman P. W. Atkins. *Molecular Quantum Mechanics, 4th edition.* OUP Oxford, 2004. 15, 38, 40, 41

[34] R. G. Parr and W. Yang. *Density-Functional Theory of Atoms and Molecules.* Oxford University Press, USA, 1989. 45

[35] M. Patanen, S. Urpelainen, M. Huttula, R. Sankari, V. Kisand, E. Nõmmiste, E. Kukk, H. Aksela, and S. Aksela. High-resolution study of K $3p$ photoabsorption and resonant auger decay in kf. *Phys. Rev. A*, 80:013414, Jul 2009. doi: 10.1103/PhysRevA.80.013414. URL http://link.aps.org/doi/10.1103/PhysRevA.80.013414. 29

[36] A. Rauk. *Orbital interaction theory of organic chemistry, 2nd edition.* John Wiley & Sons, USA, 2001. 15, 16, 17, 18

[37] C. C. J. Roothaan. New developments in molecular orbital theory. *Rev. Mod. Phys.*, 23:69–89, Apr 1951. doi: 10.1103/RevModPhys.23.69. URL http://link.aps.org/doi/10.1103/RevModPhys.23.69. 41

[38] Erich Runge and E. K. U. Gross. Density-functional theory for time-dependent systems. *Phys. Rev. Lett.*, 52:997–1000, Mar 1984. doi: 10.1103/PhysRevLett.52.997. URL http://link.aps.org/doi/10.1103/PhysRevLett.52.997. 48

[39] J. R. Schmidt, Priya V. Parandekar, and John C. Tully. Mixed quantum-classical equilibrium: Surface hopping. *The Journal of Chemical Physics*, 129(4):044104, 2008. doi: 10.1063/1.2955564. URL http://link.aip.org/link/?JCP/129/044104/1. 76

[40] Michael W. Schmidt, Kim K. Baldridge, Jerry A. Boatz, Steven T. Elbert, Mark S. Gordon, Jan H. Jensen, Shiro Koseki, Nikita Matsunaga, Kiet A. Nguyen, Shujun Su, Theresa L. Windus, Michel Dupuis, and John A. Montgomery. General atomic and molecular electronic structure system. *Journal of Computational Chemistry*, 14 (11):1347–1363, 1993. ISSN 1096-987X. doi: 10.1002/jcc.540141112. URL http://dx.doi.org/10.1002/jcc.540141112. 13

[41] J. C. Slater. The theory of complex spectra. *Phys. Rev.*, 34:1293–1322, Nov 1929. doi: 10.1103/PhysRev.34.1293. URL http://link.aps.org/doi/10.1103/PhysRev.34.1293. 39

[42] A. Szabo and N. S. Ostlund. *Modern Quantum Chemistry*. Dover Publishing, New York, 1996. 41

[43] W Tang, E Sanville, and G Henkelman. A grid-based bader analysis algorithm without lattice bias. *Journal of Physics: Condensed Matter*, 21(8):084204, 2009. URL http://stacks.iop.org/0953-8984/21/i=8/a=084204. 73

[44] Ivano Tavernelli *, Ute F. Röhrig, and Ursula Rothlisberger. Molecular dynamics in electronically excited states using time-dependent density

functional theory. *Molecular Physics*, 103(6-8):963–981, 2005. doi: 10.1080/00268970512331339378. URL http://www.tandfonline.com/doi/abs/10.1080/00268970512331339378. 65

[45] I. Tavernelli, U. F. Röhrig, and U. Rothlisberger. Molecular dynamics in electronically excited states using time-dependent density functional theory. *Molecular Physics*, 103(6-8):963–981, 2005. doi: 10.1080/00268970512331339378. URL http://www.tandfonline.com/doi/abs/10.1080/00268970512331339378. 13, 49, 50

[46] S. Urpelainen, M. Huttula, T. Balasubramanian, R. Sankari, P. Kovala, E. Kukk, E. N ommiste, S. Aksela, R. Nyholm, and H. Aksela. Finest: a high performance branch-line for vuv photon energy range gas phase studies at max-lab. *AIP Conference Proceedings*, 1234(1):411–414, 2010. doi: 10.1063/1.3463227. URL http://link.aip.org/link/?APC/1234/411/1. 29

[47] Loup Verlet. Computer "experiments" on classical fluids. i. thermodynamical properties of lennard-jones molecules. *Phys. Rev.*, 159:98–103, Jul 1967. doi: 10.1103/PhysRev.159.98. URL http://link.aps.org/doi/10.1103/PhysRev.159.98. 53

[48] W. C. Wiley and I. H. McLaren. Time-of-flight mass spectrometer with improved resolution. *Review of Scientific Instruments*, 26(12):1150–1157, 1955. doi: 10.1063/1.1715212. URL http://link.aip.org/link/?RSI/26/1150/1. 27